

# Neural Network-Based Successive Interference Cancellation for Non-Linear Bandlimited Channels

Daniel Plabst, Tobias Prinz, Francesca Diedolo, Thomas Wiegart, Georg Böcherer,  
Norbert Hanik and Gerhard Kramer

**Abstract**—Reliable communication over bandlimited and non-linear channels usually requires equalization to simplify receiver processing. Equalizers that perform joint detection and decoding (JDD) achieve the highest information rates but are often too complex to implement. To address this challenge, model-based neural network (NN) equalizers that perform successive interference cancellation (SIC) are shown to approach JDD information rates for bandlimited channels with a memoryless nonlinearity and additive white Gaussian noise. The NNs are chosen to have a periodically time-varying and recurrent structure that imitates the forward-backward algorithm (FBA) in every SIC stage. Simulations for short-haul fiber-optic links with square-law detection show that NN-SIC nearly doubles current spectral efficiencies, and bipolar or complex-valued modulations achieve energy gains of up to 3 dB compared to state-of-the-art intensity modulation. Moreover, NN-SIC is considerably less complex than equalizers that perform JDD, mismatched FBA processing, and Gibbs sampling.

**Index Terms**—intersymbol interference, neural network, non-linearity, successive interference cancellation, direct detection.

## I. INTRODUCTION

COMMUNICATION links with low transmit power are often modeled as linear intersymbol interference (ISI) channels with additive white Gaussian noise (AWGN). Orthogonal frequency division multiplexing (OFDM) converts such channels into parallel memoryless channels [1, Chap. 3.4.4], providing a practical method to approach capacity [1, Eq. 5.39]. However, device constraints or high transmit power may introduce nonlinearities at the transmitter or receiver, e.g., through a power amplifier (PA) [2], [3], or a square-law detector (SLD) [4]. Nonlinearities degrade OFDM performance [5] in general, and the receiver may need to apply joint detection and decoding (JDD) to approach capacity. Unfortunately, JDD is often too complex to implement, especially for higher-order modulation [6, Sec. IV].

A pragmatic method to reduce complexity is separate detection and decoding (SDD) for each channel input symbol; see [7], [8]. SDD rates may be significantly lower than JDD rates [6], [9]. Two methods that use SDD to approach JDD performance are turbo detection and decoding (TDD) [10]–[12] and multi-level coding (MLC) with successive interference

cancellation (SIC) [9], [13]–[15]. TDD requires a dedicated code design to approach capacity while MLC-SIC permits using off-the-shelf codes; see [14]–[16].

### A. Equalizers to Compute APPs

We focus on MLC-SIC with detectors/equalizers that output *a posteriori* probabilities (APPs) or approximations of APPs. Consider the following equalizers.

- A forward-backward algorithm (FBA) [17] that computes symbol-wise APPs. A related approach is hard- or soft-output Viterbi equalization [18], [19].
- Gibbs sampling (GS) [20, Ch. 29] as a Markov-chain, Monte-Carlo method to approximate APPs.
- Linear equalizers [6] followed by a demapper (a memoryless APP calculator).
- Nonlinear equalizers with a demapper, such as decision feedback equalizers (DFEs) [21], Volterra filters [22] and neural networks (NNs).

We compare the methods and discuss simplifications.

- The FBA outputs exact APPs but is too complex for large channel memory or modulation alphabets. One can trade off complexity and performance via mismatched models with small memory [23] or channel shortening filters [24].
- GS simplifies FBA calculations but may converge slowly at high signal-to-noise ratio (SNR), requiring many parallel samplers or iterations [9], [25].
- Linear equalizers cannot cancel nonlinearities and lose significant rate at high SNR [6, Fig. 7-9]. For example, minimum mean square error (MMSE) filtering often assumes Gaussian inputs [21], [26], [27] and is suboptimal for discrete inputs.
- Nonlinear equalizers such as DFEs exhibit error propagation [6, Fig. 10] and require decoding in the feedback path. Even with perfect feedback, MMSE-DFE [21] approaches the JDD rates only at low SNRs [6, Fig. 9]. Volterra filters are too complex [22] in general.

The main limitation of the above methods is that, for high rates, either the complexity is high or residual interference reduces rates significantly compared to JDD. We focus on model-based NN equalizers and show they can efficiently achieve high rates for large-memory models.

### B. Review of NN Receivers

We review the literature on NN receivers. For decoding, recurrent NNs (RNNs) were used to approximate the Viterbi algorithm [28], [29] and the FBA [30]–[32]. NN autoencoders

Date of current version August 28, 2024. (Corresponding author: Daniel Plabst.)

Daniel Plabst, Tobias Prinz, Francesca Diedolo, Thomas Wiegart, Norbert Hanik and Gerhard Kramer are with the Institute for Communications Engineering, School of Computation, Information, and Technology, Technical University of Munich, 80333 Munich, Germany (e-mail: daniel.plabst@tum.de; tobias.prinz@tum.de; francesca.diedolo@tum.de; thomas.wiegart@tum.de, norbert.hanik@tum.de; gerhard.kramer@tum.de). Georg Böcherer is with the Munich Research Center, Huawei Technologies Düsseldorf GmbH, 80992 Munich, Germany (e-mail: georg.bocherer@huawei.com).

were used for both turbo encoding and decoding in [33]–[38]. For equalization, we categorize papers based on whether they use JDD, SDD, TDD, or SIC.

1) *JDD*: The paper [39] performs JDD for ISI channels with two memory taps and a memoryless amplifier nonlinearity. A large receiver NN demaps and decodes polar-coded BPSK, but the approach does not scale to longer codes, and JDD cannot account for interblock interference. The works [40], [41] consider JDD for ISI channels with three memory taps and sparse code multiple access, respectively. The paper [42] proposes a JDD autoencoder for memoryless MIMO channels with few antennas. The approach is limited to small MIMO and modulation alphabets; extending to frequency-selective or massive MIMO is too complex.

2) *SDD*: The paper [43] treats ISI with separate NNs for symbol-wise APP detection and decoding. The paper [44] estimates symbol-wise APPs using NNs for millimeter wave wireless channels. The paper [45] studies OFDM with a convolutional NN for channel estimation and symbol-wise APP detection. OFDM is also considered in [46], but with feedback between the decoder and NN detector to adapt the NN to the channel state information (CSI) during a retraining phase. The paper [47] uses NNs for SDD for MIMO channels, and [48]–[50] applies NNs for SDD and long-haul fiber links. The authors of [51], [52] study short-reach fiber-optic systems with intensity modulation, SLD, and NN autoencoders.

The papers [29], [53] approximate sequence-MAP detection by NN-Viterbi detection and NN-based soft interference cancellation [54] (IC), respectively. Sequence-MAP detection is suboptimal with SDD, as the detector passes hard decisions to the decoder. For time-varying channels, both approaches may be improved by “online” retraining via a feedback path between the detector and decoder [46]. The paper [55] uses [53] for single-carrier frequency-domain equalization, where NNs are trained across different Rayleigh fading channels.

3) *TDD*: The paper [56] applies NN-TDD for ISI channels with CSI uncertainty; see [36] that also learns the component decoders. The authors of [57] propose TDD for OFDM and replace the modulator and demapper with a NN. For frequency-selective Rayleigh fading channels, autoencoding outperforms conventional OFDM due to better frequency diversity. The paper [58] studies TDD autoencoders for short packet communication and synchronization.

4) *SIC*: NNs for soft-SIC were applied to code division multiple access [59] by subtracting interference estimates between stages. NN post-processing improves the bit-error rate. NN-based SIC receivers were also applied to non-orthogonal multiple access (NOMA). The paper [60] studies the NOMA downlink with perfect CSI and replaces a soft-SIC receiver with a single NN. The paper [61] optimizes an NN-based precoder and SIC detector for NOMA with imperfect CSI. In each SIC stage, an NN estimates the data and interference from other users to subtract interference; see [61, Fig. 2]. Instead, the papers [62], [63] process the estimated interference and received channel output symbols jointly. The paper [64] performs NN-SIC for broadcast channels with imperfect CSI; each user treats the other users’ signals as noise. The APPs

are computed using soft information from prior SIC stages, similar to soft-decision feedback equalization [65].

The above works apply soft IC with no channel decoding between the stages, i.e., significant error propagation occurs if the interference is not entirely suppressed. The information rate is that of SDD.

### C. Contributions and Organization

We propose a periodically time-varying recurrent NN equalizer that is inspired by the FBA and combine it with MLC-SIC and one NN-equalizer per stage<sup>1</sup>. In contrast to the NN literature, the NN-SIC receiver decodes between stages and approaches JDD performance as the number of SIC stages increases. As a showcase, we study oversampled short-reach fiber links with long ISI and an SLD and compare the results to using mismatched FBA, SDD, and Gibbs sampling receivers [9]. Remarkably, the NN-SIC receiver outperforms and is substantially simpler than existing mismatched receivers that approximate JDD. For example, by applying the NN-SIC equalizer to bipolar and complex-valued modulation, one gains up to 3 dB in energy efficiency over classic intensity modulation, making the technique a candidate for future short-range links with direct detection.

This paper is organized as follows. Sec. II introduces the system model and Sec. III reviews SDD and SIC. Sec. IV and V discuss FBA-equalization and NN-equalization with IC, respectively. Sec. VI computes information rates for SDD and SIC receivers for short-reach fiber-optic links with a SLD and compares with [9], [23]. We find that NN-SIC substantially increases current spectral efficiencies for short-haul fiber links with SLD [9], [67]. Sec. VII concludes the paper.

### D. Notation

Column vectors and matrices are written using bold letters, e.g.,  $\mathbf{a}$ . The transpose of  $\mathbf{a}$  is  $\mathbf{a}^T$  and  $\text{cat}(\mathbf{a}, \mathbf{b}) = [\mathbf{a}^T, \mathbf{b}^T]^T$  stacks  $\mathbf{a}$  and  $\mathbf{b}$ . The real and imaginary parts of the complex number  $z$  are  $\Re\{z\}$  and  $\Im\{z\}$ , respectively. The phase of  $z$  is  $\angle z$ . We denote strings of scalars and vectors by  $x_\kappa^n = (x_\kappa, \dots, x_n)$  and  $\mathbf{X}_\kappa^n = (\mathbf{X}_\kappa, \dots, \mathbf{X}_n)$ , respectively, and omit the subscript if  $\kappa = 1$ . For positive integers  $a, b, c, d$ , we use the notation  $(x_{\kappa,u})_{a \leq \kappa \leq b, c \leq u \leq d}$  to denote the string  $(x_{\kappa,u} \mid a \leq \kappa \leq b, c \leq u \leq d)$ .

Random variables (RVs) are written in uppercase letters, and their realizations in lowercase. The probability mass function (PMF) and density of a vector of discrete and continuous RVs  $\mathbf{X}$  is written as  $P_{\mathbf{X}}$  and  $p_{\mathbf{X}}$ , respectively. We often discard subscripts on PMFs or densities if the arguments are uppercase or lowercase versions of their RVs. The conditional PMF of a discrete RV  $X$  given  $Y$  is  $P_{X|Y}$ . Similarly, we use  $P_{X|Y}(\cdot|y)$  for the PMF of  $X$  given  $Y = y$ .

The sinc function is  $\text{sinc}(t) = \sin(\pi t)/(\pi t)$ . The convolution of  $g(t)$  and  $h(t)$  is  $g(t) * h(t)$  and the energy of  $a(t)$  is  $\|a(t)\|^2 = \int_{-\infty}^{\infty} |a(t)|^2 dt$ . Entropy, conditional entropy, and mutual information are defined as in [68, Chap. 2], and we measure the quantities in bits.

<sup>1</sup>A conference version of this manuscript is available at [66].

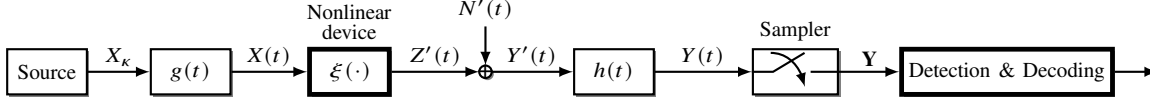


Fig. 1. Bandlimited channel with a memoryless nonlinear device and additive noise.

## II. SYSTEM MODEL

We study bandlimited channels with a memoryless nonlinear device  $\xi(\cdot)$  and additive noise, as shown in Fig. 1. For example, this model applies to wireless communications with nonlinearities at the transmitter due to PAs, mixers, and digital-to-analog converters (DACs) [2], [3], or at the receiver due to low-noise amplifiers (LNAs), mixers, and analog-to-digital converters (ADCs). The model also describes fiber-optic communications with nonlinearities at the transmitter due to a driver amplifier, DAC, Mach-Zehnder modulator, and optical amplifiers, or at the receiver with a square-law detector (SLD), a single photodiode [23, Fig. 2], LNA, and ADC.

Fig. 1 assumes additive noise  $N'(t)$  after the nonlinearity. For instance,  $N'(t)$  might model the amplified thermal noise of a radio-frequency amplifier [69]–[72], or the amplified spontaneous emission noise of an erbium-doped fiber amplifier, or the lumped noise of photo-detection [73, Sec. II], the LNA, and the ADC.

### A. Continuous Time Model

The source in Fig. 1 generates uniformly, independently and identically distributed (u.i.i.d.) symbols  $(X_k)_{k \in \mathbb{Z}} = (\dots, X_1, X_2, X_3, \dots)$  from the symbol alphabet  $\mathcal{A} = \{a_1, \dots, a_M\}$  where  $M = 2^m$ . After filtering with  $g(t)$ , the baseband waveform is

$$X(t) = \sum_{\kappa} X_{\kappa} \cdot g(t - \kappa T_s) \quad (1)$$

where  $B = 1/T_s$  is the symbol rate and  $g(t)$  collects all linear effects, including the bandwidth limitations of the pulse, nonlinear device, and DAC. The nonlinear device puts out  $Z'(t) = \xi(X(t))$  to which noise  $N'(t)$  is added. The noise is modeled as a complex white Gaussian random process with two-sided power spectral density (PSD)  $N_0/2$  Watts per Hertz per dimension.

The signal and noise are filtered by  $h(t)$ , which may include a receiver bandwidth limitation and anti-aliasing filter matched to the ADC. Fig. 1 can also be extended to colored noise using an additional whitening filter as the front-end of  $h(t)$ . The filtered noise  $N(t) = N'(t) * h(t)$  is a stationary circularly-symmetric complex Gaussian process with autocorrelation function (ACF)

$$\varphi_{NN}(\tau) = N_0 \cdot (h^*(-\tau) * h(\tau)). \quad (2)$$

Next, we describe the effect of the nonlinear device on  $X(t)$ .

### B. Memoryless Nonlinear Device

The nonlinearity expands the bandwidth, e.g., if  $\xi(\cdot)$  is a polynomial of degree  $d_{\xi}$  then  $Z'(t)$  occupies  $d_{\xi}$  times

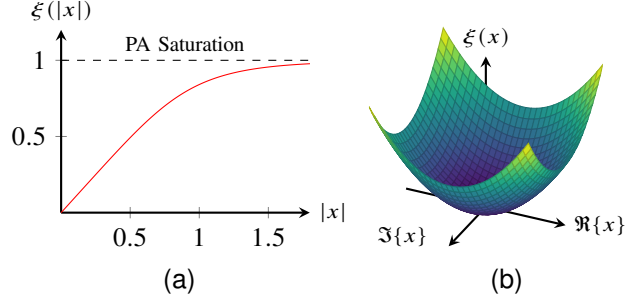


Fig. 2. Nonlinear functions for a (a) PA:  $\xi(|x|) = |x|/\sqrt[4]{1+|x|^4}$  and (b) SLD:  $\xi(x) = |x|^2$ .

the bandwidth of  $X(t)$  [74, Sec. 3.1], [75, Thm. 1]. More generally, the bandwidth of  $Z'(t)$  may be unbounded but is bandlimited via  $h(t)$ . We consider the two applications with the nonlinear functions shown in Fig. 2.

1) *Wireless Transmitter with a PA*: The model in [76, Fig. 1] has

$$Z'(t) = \xi(|X(t)|) \cdot \exp(j\angle X(t)) \quad (3)$$

with a nonlinear real-valued function  $\xi(\cdot)$  that models a solid-state PA that distorts the magnitude; see [70, Sec. 3.2].

2) *Optical Fiber Receiver with a SLD*: The model in [23, Fig. 2] has a single polarization and  $g(t) \propto \text{sinc}(Bt) * g_{\text{SSMF}}(t)$  where  $g_{\text{SSMF}}(t)$  is the linear response (dispersion) of a standard single-mode fiber (SSMF). The SLD outputs  $\xi(\cdot) = |\cdot|^2$  and the front-end of the ADC is a brickwall filter  $h(t) \propto \text{sinc}(2Bt)$  with twice the transmit filter bandwidth.

### C. Discrete Time Model

One obtains a discrete time model by collecting samples  $Y_k = Y(kT'_s)$ ,  $k \in \mathbb{Z}$ , where  $T'_s = 1/(BN_{\text{os}})$  corresponds to sampling at rate  $BN_{\text{os}}$  with oversampling factor  $N_{\text{os}}$ . The Nyquist-Shannon sampling theorem is met if  $Y(t)$  is bandlimited and  $N_{\text{os}}$  is sufficiently high. The  $k^{\text{th}}$  sample is

$$Y_k = Z_k + N_k \quad (4)$$

where

$$Z_k = [h(t) * \xi(X(t))]_{t=kT'_s} \quad (5)$$

$$N_k = [h(t) * N'(t)]_{t=kT'_s}. \quad (6)$$

The discrete-time noise  $N_k$  is stationary, circularly symmetric, and complex Gaussian with ACF

$$\varphi_{NN}[k] = N_0 \cdot \varphi_{NN}(\tau = kT'_s). \quad (7)$$

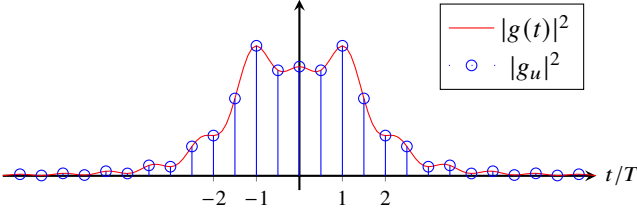


Fig. 3. Magnitude-squared response of an SSMF channel with parameters in Tab. II, length 30 km and  $g(t) \propto \text{sinc}(Bt) * g_{\text{SSMF}}(t)$ ; circles show samples with  $N_{\text{sim}} = 2$ .

#### D. Approximation via Simulation

We use oversampling to address the bandwidth expansion. Let  $T_{\text{sim}} = T_s/N_{\text{sim}}$  be the simulation sampling period where  $N_{\text{sim}}$  is the simulation oversampling factor and  $d = N_{\text{sim}}/N_{\text{os}}$  is a positive integer. One can approximate

$$Z_k \approx \sum_{u'} h_{u'} \xi \left( \sum_u g_u X'_{(d \cdot k - u') - u} \right) \quad (8)$$

where  $(X'_u)_{u \in \mathbb{Z}} = ((0, \dots, 0, X_k))_{k \in \mathbb{Z}}$  is a  $N_{\text{sim}}$ -fold upsampled string, and  $g_u = g(uT_{\text{sim}})$ ,  $h_u = h(uT_{\text{sim}})$  are the oversampled filters. The SLD example above has  $d_{\xi} = 2$  and  $N_{\text{os}} = N_{\text{sim}} = 2$  results in sufficient statistics, and (8) is an equality. However, if the PA model in (3) is not a polynomial, then one may need to choose a large  $N_{\text{sim}}$  so that (8) is a good approximation.

To illustrate, suppose the filters  $g_u$  and  $h_u$  in (8) have odd lengths  $K_g$  and  $K_h$ , respectively, and the filter taps are zero outside the intervals  $[-\lfloor K_g/2 \rfloor, \lfloor K_g/2 \rfloor]$  and  $[-\lfloor K_h/2 \rfloor, \lfloor K_h/2 \rfloor]$ . The filters have symbol memories  $\tilde{K}_g = \lfloor (K_g - 1)/N_{\text{sim}} \rfloor$  and  $\tilde{K}_h = \lfloor (K_h - 1)/N_{\text{sim}} \rfloor$ , and the total system memory is

$$\tilde{K} = \tilde{K}_g + \tilde{K}_h. \quad (9)$$

For example, Fig. 3 shows a bandlimited SSMF channel  $g(t)$  with memory  $\tilde{K}_g = 13$ .

We use block transmission with  $\lfloor K_g/2 \rfloor + \lfloor K_h/2 \rfloor$  zeros at the beginning and end of each block. We collect a block of  $n$  transmit symbols in the vector

$$\mathbf{x} = [x_1, x_2, x_3, \dots, x_n]^T \in \mathbb{C}^n. \quad (10)$$

The receiver collects  $N_{\text{os}}$  channel output symbols per transmitted symbol in the vector

$$\mathbf{y} = [y_1, y_2, y_3, \dots, y_{N_{\text{os}}n}]^T \in \mathbb{C}^{N_{\text{os}}n}. \quad (11)$$

### III. SDD AND SIC RATES

This section derives information rates with SDD and SIC; see [9, Sec. IV A-B].

#### A. SDD Rates

SDD computes the symbol-wise APPs  $P_{X_\kappa|\mathbf{Y}}(\cdot|\mathbf{y})$ ,  $\kappa \in \{1, \dots, n\}$ , and the decoder uses these to estimate the data. Consider the entropy rates

$$H_n(\mathbf{X}) = \frac{1}{n} H(\mathbf{X}) \quad (12)$$

$$H_n(\mathbf{X}|\mathbf{Y}) = \frac{1}{n} H(\mathbf{X}|\mathbf{Y}). \quad (13)$$

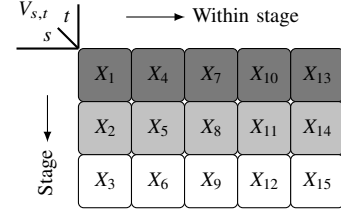


Fig. 4. SIC with  $S = 3$  stages and  $n = 15$  input symbols.

A lower bound on the information rate of  $\mathbf{X}$  and  $\mathbf{Y}$  is:

$$I_n(\mathbf{X}; \mathbf{Y}) = H_n(\mathbf{X}) - H_n(\mathbf{X}|\mathbf{Y}) \quad (14)$$

$$\geq H_n(\mathbf{X}) - \frac{1}{n} \sum_{\kappa=1}^n H(X_\kappa|\mathbf{Y}) := I_{n,\text{SDD}} \quad (15)$$

with equality if and only if  $X_\kappa$  and  $X^{\kappa-1}$  are conditionally independent given  $\mathbf{Y}$ . Define the limiting rates as

$$I(\mathcal{X}; \mathcal{Y}) := \lim_{n \rightarrow \infty} I_n(\mathbf{X}; \mathbf{Y}), \quad I_{\text{SDD}} := \lim_{n \rightarrow \infty} I_{n,\text{SDD}} \quad (16)$$

and note that the bound (15) gives  $I_{\text{SDD}} \leq I(\mathcal{X}; \mathcal{Y})$ .

JDD achieves the rate  $I(\mathcal{X}; \mathcal{Y})$ , but is usually too complex to implement [77]–[79]. In practice, one is often limited to SDD and the rate  $I_{\text{SDD}}$ , but [6, Fig. 7-9] and [9, Fig. 6] show that SDD loses significant rate for ISI channels at medium to high SNRs. This is because SDD neglects stochastic dependencies when computing APPs of systems with memory.

#### B. SIC Rates

SIC increases the SDD rates and is implemented with  $S$  stages and a different forward error control (FEC) code for each stage [14].

1) *SIC Encoding*: To encode, downsample  $\mathbf{X}$  by a factor of  $S$  to create  $S$  sequences of length  $N = n/S$ , where we assume  $N$  is an integer. The symbols in the  $s^{\text{th}}$  SIC stage are

$$\mathbf{V}_s = (V_{s,t})_{t=1}^N = (X_{\kappa(s,1)}, X_{\kappa(s,2)} \dots X_{\kappa(s,N)}) \quad (17)$$

where  $\kappa(s, t) = s + (t - 1)S$  converts a parallel indexing  $(s, t)$  to a serial indexing  $\kappa(s, t)$ . For example, consider Fig. 4 with  $S = 3$ ,  $n = 15$ ,  $N = 5$ , and thus

$$\mathbf{V}_1 = (X_1, X_4, X_7, X_{10}, X_{13}). \quad (18)$$

2) *SIC Receiver*: We detect and decode using  $S$  stages; see Fig. 5. To illustrate, consider again  $S = 3$  and partition  $\mathbf{X}$  into  $\mathbf{V}_1, \mathbf{V}_2, \mathbf{V}_3$ . The first stage performs SDD and calculates the APPs  $P_{V_{1,t}|\mathbf{Y}}(\cdot|\mathbf{y})$  for  $t = 1, \dots, N$ . A decoder estimates  $\hat{\mathbf{V}}_1$ . The second stage uses  $\hat{\mathbf{V}}_1$  as prior information and calculates the APPs  $P_{V_{2,t}|\mathbf{V}_1, \mathbf{Y}}(\cdot|\hat{\mathbf{v}}_1, \mathbf{y})$  for  $t = 1, \dots, N$ . Correct prior information increases the information rate in the second SIC stage. The final stage computes the APPs  $P_{V_{3,t}|\mathbf{V}_1, \mathbf{V}_2, \mathbf{Y}}(\cdot|\hat{\mathbf{v}}_1, \hat{\mathbf{v}}_2, \mathbf{y})$  for  $t = 1, \dots, N$ .

3) *SIC Rates*: Define the long string  $\mathbf{V} = (\mathbf{V}_s)_{s=1}^S$ . Since  $\mathbf{V}$  is a reordered version of  $\mathbf{X}$ , we have  $I_n(\mathbf{X}; \mathbf{Y}) = I_n(\mathbf{V}; \mathbf{Y})$ . The rate of stage  $s$  is

$$I_{n,\text{SIC}}^s = \frac{1}{N} \sum_{t=1}^N I(V_{s,t}; \mathbf{Y}, \mathbf{V}^{s-1}) \quad (19)$$

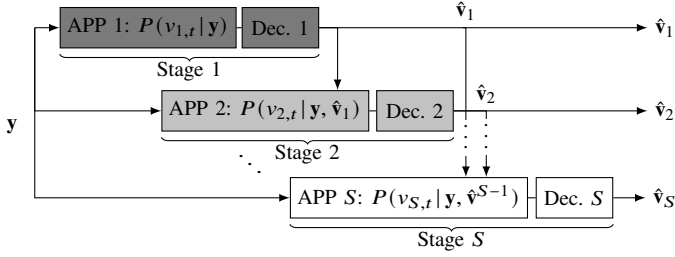


Fig. 5. SIC receiver with SDD for each stage.

and  $I_{N,\text{SIC}}^s$  is non-decreasing in  $s$  and is at most  $m$ . The average SIC rate is

$$I_{n,\text{SIC}} = \frac{1}{S} \sum_{s=1}^S I_{N,\text{SIC}}^s \quad (20)$$

and satisfies

$$I_{n,\text{SDD}} \leq I_{n,\text{SIC}} \leq I_n(\mathbf{V}; \mathbf{Y}). \quad (21)$$

Define  $I_{\text{SIC}}^s := \lim_{N \rightarrow \infty} I_{N,\text{SIC}}^s$  and  $I_{\text{SIC}} := \lim_{n \rightarrow \infty} I_{n,\text{SIC}}$ . We encode  $\mathbf{V}_s$  with a code rate less than  $I_{\text{SIC}}^s$  to ensure reliable decoding as the block length grows, i.e., we may assume  $\hat{\mathbf{V}}_s = \mathbf{V}_s$ ; see [14]. Comparing the limiting rates, we obtain

$$I_{\text{SDD}} \leq I_{\text{SIC}} \leq I(\mathcal{X}; \mathcal{Y}). \quad (22)$$

SIC can approach the JDD performance by increasing  $S$  [9, Fig. 6]. Also,  $S$  should increase with the total memory  $\tilde{K}$  (9), modulation alphabet size, and ISI magnitude; see [9, Sec. IV B and Fig. 2] on how the effective memory is reduced at higher SIC stages.

#### IV. FBA EQUALIZER

A SIC receiver requires symbol-wise APP calculations at each stage. We extend the APP calculations in [23, Sec. III-IV] from SDD to SIC. In particular, we show how the APPs of Fig. 5 are computed via the FBA. The FBA structure is later used to design model-based NNs.

Consider the channel outputs  $\check{y}_k := y_{k-k_0}$ , where  $k_0 = \lfloor \lfloor K_g/2 \rfloor / d + \lfloor \lfloor K_h/2 \rfloor / d \rfloor$  and  $d = N_{\text{sim}}/N_{\text{os}}$ ; see Sec. II-D. We collect  $N_{\text{os}}$  output symbols per input  $X_\kappa$  in the string

$$\check{\mathbf{y}}_\kappa := (\check{y}_{\kappa+N_{\text{os}}(\kappa-1)+\ell})_{\ell=0}^{N_{\text{os}}-1}. \quad (23)$$

For SIC stage  $s$ ,  $s \in \{1, \dots, S\}$ , the FBA computes the APPs

$$P_{V_{s,t}|\check{\mathbf{y}}, \mathbf{v}^{s-1}}(\cdot|\check{\mathbf{y}}, \mathbf{v}^{s-1}) \quad \forall t \quad (24)$$

where  $\check{\mathbf{y}} := (\check{y}_1, \dots, \check{y}_n)$ . Fig. 6 depicts the FBA structure by a factor graph. SDD has  $S = 1$ ; see [23, Fig. 4].

We increase the memory  $\tilde{K}$  so that  $\tilde{K}/S$  is an integer to simplify the analysis. Now partition the channel state (the past  $\tilde{K}$  input symbols) into disjoint strings for  $j = 1, \dots, S$ :

$$H_{j,t} := (X_{\kappa(j,t)-\ell})_{\ell=0}^{\tilde{K}-1} \setminus \mathbf{V}^{s-1} \quad (25)$$

$$H_{j,t}^c := (X_{\kappa(j,t)-\ell})_{\ell=0}^{\tilde{K}-1} \setminus H_{j,t} \quad (26)$$

where  $H_{j,t}$  has  $\tilde{K}_s = (S-s+1) \cdot \tilde{K}/S$  unknown symbols and  $H_{j,t}^c$  has  $\tilde{K}_s^c = (s-1) \cdot \tilde{K}/S$  known symbols. For example, consider  $\tilde{K} = 3$ ,  $S = 3$ , and  $s = 2$ , for which  $\tilde{K}_s = 2$ ,  $\tilde{K}_s^c = 1$ , the known symbols are  $\mathbf{V}^{s-1} = X_1, X_4, X_7, \dots$ , and thus

$$H_{j,t}, H_{j,t}^c = \begin{cases} (X_2, X_3), (X_1) & j = 3, t = 1 \\ (X_2, X_3), (X_4) & j = 1, t = 2 \\ (X_3, X_5), (X_4) & j = 2, t = 2 \\ (X_5, X_6), (X_4) & j = 3, t = 2 \\ \vdots & \end{cases} \quad (27)$$

For  $s > 1$ , one may simplify by marginalizing only over the states  $H_{j,t}$ . Note that the states  $H_{S,t}, H_{1,t+1}, \dots, H_{s-1,t+1}$  are the same for all  $t$ , as the channel inputs from time steps  $\kappa(1, t)$  to  $\kappa(s-1, t+1)$  are known; see (27). The factor graph in Fig. 6 thus uses only  $H_{S,t}$ . The FBA complexity decreases with increasing  $s$  because the effective memory  $\tilde{K}_s$  decreases with  $s$ .

For each stage  $s$ , the FBA computes APPs by processing on Fig. 6 over two paths. The first path runs forward in time and recursively calculates forward state metrics, while the second path runs backward in time and computes backward state metrics. Both paths use decoded symbols  $\mathbf{V}^{s-1} = \mathbf{v}^{s-1}$  from previous SIC stages. Define the respective forward and backward state metrics for  $j = s, s+1, \dots, S$  as

$$\tilde{\mu}_{j,t}(h_{j,t}) := p(\check{\mathbf{y}}_1^{\kappa(j,t)}, (v_{u,\ell})_{1 \leq u < s, 1 \leq \ell \leq t}, h_{j,t}) \quad (28)$$

$$\tilde{\mu}_{j,t}(h_{j,t}) := p(\check{\mathbf{y}}_{\kappa(j,t)+1}^n, (v_{u,\ell})_{1 \leq u < s, t < \ell \leq N} \mid h_{j,t}, h_{j,t}^c). \quad (29)$$

The APPs for stage  $s$ , for all  $t$ , and  $a \in \mathcal{A}$  are obtained by

$$P_{V_{s,t}|\check{\mathbf{y}}, \mathbf{v}^{s-1}}(a|\check{\mathbf{y}}, \mathbf{v}^{s-1}) \propto \sum_{h_{s,t}: v_{s,t}=a} \tilde{\mu}_{s,t}(h_{s,t}) \cdot \tilde{\mu}_{s,t}(h_{s,t}). \quad (30)$$

Finally, the forward and backward state metrics are calculated recursively via (31)-(32) on the bottom of the next page, where

$$\psi_{j,t}(h_{j,t}, h_{j-1,t}, v_{j,t}) = p(\check{\mathbf{y}}_{\kappa(j,t)}, h_{j,t}, v_{j,t} \mid h_{j-1,t}, h_{j-1,t}^c) \quad (33)$$

and the expression  $\psi'_t(a)$  is

$$\prod_{j=1}^{s-1} P_{\check{\mathbf{y}}_{\kappa(j,t)}|H_{j-1,t}, H_{j-1,t}^c, v_{j,t}}(\check{\mathbf{y}}_{\kappa(j,t)} \mid a, h_{j-1,t}^c, v_{j,t}). \quad (34)$$

where index pairs are mapped as

$$\left. \begin{matrix} (0, t) \\ (s-1, t) \end{matrix} \right\} \mapsto (S, t-1) \quad (35)$$

because of the parallel indexing; see Fig. 4 and the factor graph in Fig. 6. We compare the recursions (31)-(32) to the classic FBA in [23, Sec. III-IV] for different  $s$ :

- For  $s = 1$  we have  $\psi'_t(\cdot) = 1$  and (33) is independent of the index  $j \in \{1, \dots, S\}$ . Thus, the state recursions are also independent of  $j \in \{1, \dots, S\}$ . This corresponds to the classic FBA [23, Sec. III-IV] that performs time-invariant state recursions.
- For  $1 < s < S$ , the state recursions vary with  $j \in \{s, \dots, S\}$  due to the  $j$ -dependency of (33) and the

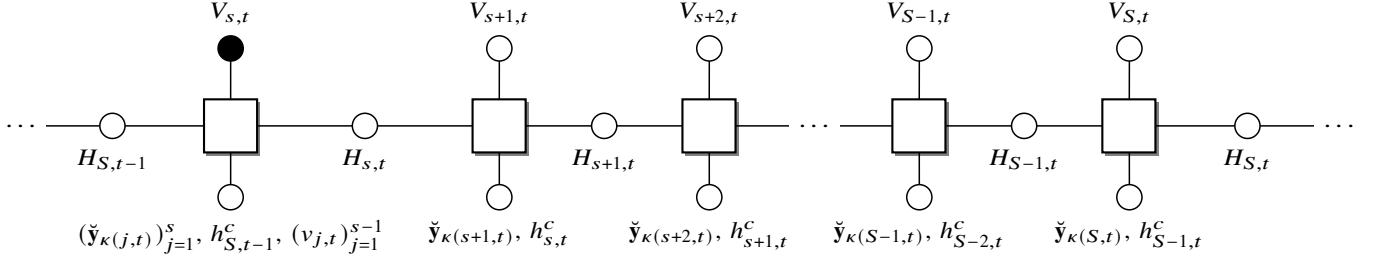


Fig. 6. Factor graph for the FBA in stage  $s$ . The string  $(v_{j,t})_{j=1}^{s-1}$  represents known symbols. Due to previous SIC levels, the  $h_{j,t}^c$ ,  $j \in \{s, \dots, S\}$ , are known parts of the channel state. The first state index takes on values in  $\{s, \dots, S\}$ . The filled variable node marks a symbol for which an APP is calculated.

additional factor (34). The FBA uses periodically time-varying state recursions.

- For  $s = S$ , the FBA applies only the first case of (31) and (32), respectively, which results in time-invariant recursions

Note that the first cases of (31) and (32) include the factor (34) that depends on known symbols  $(v_{j,t})_{j=1}^{s-1}$ ; cf. the example (27). The first forward and last backward state metrics are initialized with symbols drawn from a uniform distribution.

## V. NN EQUALIZER

The FBA is too complex to implement even for relatively small memory  $\tilde{K}$  or alphabets  $\mathcal{A}$ , so one must use mismatched models. In every SIC stage  $s$ , we use NN-equalizers with an FBA structure that are bidirectional, recurrent, and periodically time-varying.

### A. NN Inputs and Outputs

Fig. 7 shows an NN equalizer with multiple layers. Each layer is bidirectional with a forward and backward path and internal states similar to the FBA [30]–[32]. The layers imitate message passing on the factor graph of Fig. 6. We found that processing the inputs (23) successively, as in the FBA, requires many RNN states that store soft information about previous inputs. To reduce the number of states, the first NN layer effectively acts as a (nonlinear) channel shortening filter [24] that processes overlapping blocks of channel outputs and SIC symbols. The NN layers may be interpreted as turbo detection and decoding modules exchanging extrinsic information [16]. We next discuss the NN for SIC stage  $s$ .

1) *Inputs*: Suppose the NN inputs are real-valued. (One may also use complex-valued inputs; the choice is not crucial to the performance.) In SIC stage  $s$ , we process inputs for the remaining stages  $j = s, \dots, S$ ; cf. the FBA recursions (31) and (32). Define

$$\mathbf{r}_{j,t}^1 := (\bar{\mathbf{y}}_{j,t}, \bar{\mathbf{v}}_{j,t}) \in \mathbb{R}^{L_Y + L_{IC}} \quad (36)$$

with  $L_{IC}$  symbols  $\bar{\mathbf{v}}_{j,t}$  and  $L_Y$  channel outputs

$$\bar{\mathbf{v}}_{j,t} := (y_{N_{os} \cdot \kappa(j,t) + u})_{u=-\Delta}^{\nabla} \in \mathbb{R}^{L_Y} \quad (37)$$

where  $\Delta := \lfloor (L_Y - 1)/2 \rfloor$  and  $\nabla := \lceil (L_Y - 1)/2 \rceil$  correspond to symbols before and after transmission of the symbol  $v_{j,t} = x_{\kappa(j,t)}$ , respectively. Next, collect the  $L_{IC}$  symbols among  $\mathbf{v}^{s-1}$  that are closest to  $v_{j,t} = x_{\kappa(j,t)}$  in the vector

$$\bar{\mathbf{v}}_{j,t} := (x_{\kappa} \mid \kappa \in \mathcal{V}_{j,t}) \in \mathbb{R}^{L_{IC}} \quad (38)$$

where by “closest” we mean

$$\mathcal{V}_{j,t} = \operatorname{argmin}_{|\mathcal{U}|=L_{IC}} \sum_{a \in \mathcal{U}} \min_{x_a \in \mathbf{v}^{s-1}} |a - \kappa(j,t)|. \quad (39)$$

Selecting the IC symbols (38) is useful for symmetric impulse responses where  $|g_u|^2$  is nearly maximum at  $u = 0$  and decreases with  $|u|$  beyond some threshold; see Fig. 3. We use zero-padding to extend the vectors (37) where necessary.

2) *Outputs*: After processing the  $(\mathbf{r}_{j,t}^1)_{j=s}^S$  in (36) for all  $t$ , the RNN outputs APP estimates for the current stage  $s$ :

$$Q_{V_{s,t} | \mathbf{Y}, \mathbf{v}^{s-1}}(\cdot \mid \mathbf{y}, \mathbf{v}^{s-1}) \quad \forall t. \quad (40)$$

$$\text{Forward recursion: } \tilde{\mu}_{j,t}(h_{j,t}) = \begin{cases} \sum_{h_{j-1,t}, v_{j,t}} \tilde{\mu}_{j-1,t}(h_{j-1,t}) \cdot \psi_{j,t}(h_{j,t}, h_{j-1,t}, v_{j,t}) \cdot \psi'_t(h_{j-1,t}), & j = s \\ \sum_{h_{j-1,t}, v_{j,t}} \tilde{\mu}_{j-1,t}(h_{j-1,t}) \cdot \psi_{j,t}(h_{j,t}, h_{j-1,t}, v_{j,t}), & j = s+1, \dots, S \end{cases} \quad (31)$$

$$\text{Backward recursion: } \tilde{\mu}_{j-1,t}(h_{j-1,t}) = \begin{cases} \sum_{h_{j,t}, v_{j,t}} \tilde{\mu}_{j,t}(h_{j,t}) \cdot \psi_{j,t}(h_{j,t}, h_{j-1,t}, v_{j,t}) \cdot \psi'_t(h_{j-1,t}), & j = s \\ \sum_{h_{j,t}, v_{j,t}} \tilde{\mu}_{j,t}(h_{j,t}) \cdot \psi_{j,t}(h_{j,t}, h_{j-1,t}, v_{j,t}), & j = s+1, \dots, S \end{cases} \quad (32)$$

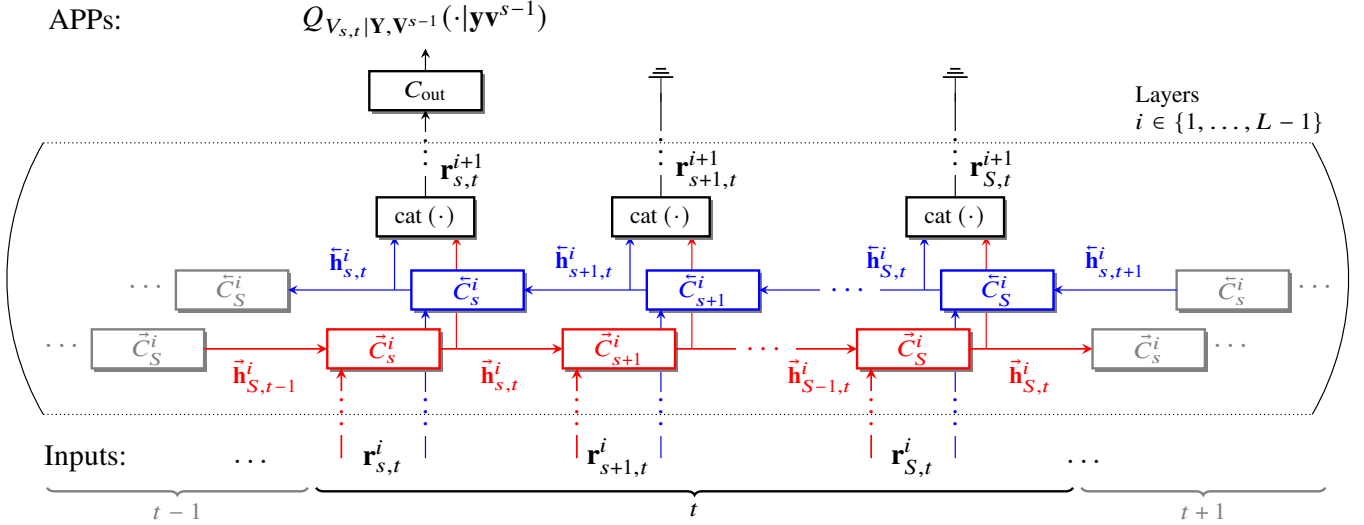


Fig. 7. Bidirectional time-varying RNN for stage  $s$ .

### B. RNN Structure

The RNN processes its inputs in forward and backward chronological orders:

$$\begin{array}{ccccccc} \dots & \mathbf{r}_{s,t}^1 & , & \mathbf{r}_{s+1,t}^1 & , & \dots & , & \mathbf{r}_{S,t}^1 \\ & \mathbf{r}_{s,t+1}^1 & , & \mathbf{r}_{s+1,t+1}^1 & , & \dots & , & \mathbf{r}_{S,t+1}^1 \end{array} \quad \dots \quad (41)$$

Stage  $s$  processes a total of  $N(S-s+1)$  inputs; see Fig. 7.

The process producing (41) is stationary. This means that for  $s > 1$ , the sub-process for stages  $s$  to  $S$  in (41) is cyclostationary with period  $\Gamma = S-s+1$  due to the SIC partitioning of Sec. III-B. We now encounter the following issue. Classic RNNs [80, Chap. 10.3] use time-invariant input and state processing, but such RNNs can perform poorly with cyclostationary inputs; see [80, p. 390]. Motivated by the FBA state recursions (31)-(32), which are periodically time-varying for  $s > 1$  with period  $\Gamma$ , we allow periodically time-varying input processing and state recursions in the RNN. For  $s = 1$ , the process (41) is stationary and the FBA recursions (31)-(32) are time-invariant; in this case we may use the classic RNNs [80, Chap. 10.3] for which  $\Gamma = 1$ . Fig. 7 shows the structure of such a bidirectional RNN with  $L$  layers:  $L-1$  layers are recurrent with forward and backward paths, and the last layer is feedforward.

Consider the forward path in layer  $i$ . This path has cells  $\tilde{C}_s^i, \tilde{C}_{s+1}^i, \dots, \tilde{C}_S^i$  that repeat periodically for  $t = 1, \dots, N$ , just like the node in the factor graph in Fig. 6. Compared to classic RNNs, the number of RNN parameters increases by a factor of  $\Gamma$ , but the computational complexity remains the same [80, Chap. 10.3]. RNNs have internal states  $(\tilde{\mathbf{h}}_{j,t}^i)_{j=s}^S$  in the forward and backward paths, where  $t = 1, \dots, N$ .

To illustrate further, let the input dimensions of the recurrent layers and the output layer be  $(\ell_1, \dots, \ell_{L-1}, \ell_L)$ , where  $\ell_1 = L_Y + L_{IC}$ . We convert the pairs (36) to column vectors. The state recursion via the cell  $\tilde{C}_j^i$ ,  $j = s, \dots, S$ , is

$$\tilde{\mathbf{h}}_{j,t}^i = f(\tilde{\mathbf{W}}_{in,j}^i(\mathbf{r}_{j,t}^i) + \tilde{\mathbf{W}}_{j-1}^i(\tilde{\mathbf{h}}_{j-1,t}^i)) \in \mathbb{R}^{\ell_{i+1}/2} \quad (42)$$

where  $f(\cdot)$  is the per-entry rectified linear unit (ReLU) [81] and we use the mapping (35) and  $s-1 \mapsto S$  for the parallel indexing. The input and state maps for  $j = s, \dots, S$  are

$$\begin{array}{ll} \tilde{\mathbf{W}}_{in,j}^i : \mathbb{R}^{\ell_i} \mapsto \mathbb{R}^{\ell_{i+1}/2}, & \tilde{\mathbf{W}}_{in,j}^i(\mathbf{r}_{j,t}^i) = \tilde{\mathbf{W}}_{in,j}^i \mathbf{r}_{j,t}^i + \tilde{\mathbf{b}}_{in,j}^i \\ \tilde{\mathbf{W}}_j^i : \mathbb{R}^{\ell_{i+1}/2} \mapsto \mathbb{R}^{\ell_{i+1}/2}, & \tilde{\mathbf{W}}_j^i(\tilde{\mathbf{h}}_{j,t}^i) = \tilde{\mathbf{W}}_j^i \tilde{\mathbf{h}}_{j,t}^i + \tilde{\mathbf{b}}_j^i \end{array}$$

where  $\tilde{\mathbf{W}}_{in,j}^i, \tilde{\mathbf{W}}_j^i$  are input and state recursion matrices, and  $\tilde{\mathbf{b}}_{in,j}^i, \tilde{\mathbf{b}}_j^i$  are input and state bias vectors, respectively. The backward path works analogously; see Fig. 7.

To complete the recurrent layer processing, the outputs of the two paths are concatenated for  $j = s, \dots, S$  and all  $t$ :

$$\mathbf{r}_{j,t}^{i+1} = \text{cat}(\tilde{\mathbf{h}}_{j,t}^i, \tilde{\mathbf{h}}_{j,t}^i) \in \mathbb{R}^{\ell_{i+1}} \quad (43)$$

and (43) is passed to the next recurrent layer if  $i+1 < L$ . If  $i+1 = L$ , the last cell  $C_{out}$  performs final processing, i.e., for all  $t$  and fixing  $j = s$  we have

$$Q_{V_{s,t}|Y, V^{s-1}}(\cdot | \mathbf{y}, \mathbf{v}^{s-1}) = \phi(\mathbf{W}_{out} \mathbf{r}_{s,t}^L + \mathbf{b}_{out}) \in \mathbb{R}^{|\mathcal{A}|} \quad (44)$$

where  $\mathbf{W}_{out} \in \mathbb{R}^{|\mathcal{A}| \times \ell_L}$ ,  $\mathbf{b}_{out} \in \mathbb{R}^{|\mathcal{A}|}$ , and the ‘‘softmax’’ function  $\phi(\cdot)$  [82] generates a PMF interpreted as symbol-wise APPs. To initialize the RNN, we set the first forward and last backward states in all recurrent layers to zero.

### C. Achievable Rates and NN Optimization

The NN-equalizers approximate APPs via (44), which gives a lower bound on the SIC rate (see [9, Sec. VI D.], [83]):

$$I_{n,SIC} \geq \underbrace{\frac{1}{S} \sum_{s=1}^S \frac{1}{N} \sum_{t=1}^N H(V_{s,t}) + \mathbb{E}[\log_2 Q(V_{s,t} | \mathbf{Y}, \mathbf{V}^{s-1})]}_{:= I_{q,N,SIC}^S} \quad (45)$$

where the expectation is over the actual  $p_{V_{s,t}, \mathbf{Y}, \mathbf{V}^{s-1}}$ . The expression  $I_{q,N,SIC}^S$  is the mismatched rate of SIC stage  $s$  and we define the limiting rate as  $I_{q,SIC}^S := \lim_{N \rightarrow \infty} I_{q,N,SIC}^S$ .

TABLE I  
ALGORITHMIC COMPLEXITY PER APP ESTIMATE.

Algorithm	Multiplications
FBA [23]	$O(S \cdot  \mathcal{A} ^{\tilde{K}+1})$
Bit-wise GS [9]	$O(S \cdot \tilde{K}^2 \cdot m \cdot N_{\text{iter}} \cdot N_{\text{par}})$
NN	$O(S \cdot (\sum_{i=1}^{L-1} \ell_i \ell_{i+1} + \ell_{i+1}^2/2 + \ell_L \cdot  \mathcal{A} ))$

We wish to maximize  $I_{q,N,\text{SIC}}^s$ , or equivalently minimize the expectation in (45) (a cross entropy) for each SIC stage  $s$ . To simplify notation, collect the NN parameters (the NN weights and biases) in a string  $\Theta$ . We estimate  $I_{q,N,\text{SIC}}^s$  via simulation and formulate the optimization problem [84, Sec. 4.1] as

$$\begin{aligned} \underset{(\mathcal{Q}_{V_{s,t}|\mathbf{Y},\mathbf{V}^{s-1}})_{t=1}^N}{\text{argmin}} \quad & -\frac{1}{N} \sum_{t=1}^N \left\langle \log_2 \mathcal{Q}_{V_{s,t}|\mathbf{Y},\mathbf{V}^{s-1}}(v_{s,t} | \mathbf{y}, \mathbf{v}^{s-1}) \right\rangle \\ \text{subject to} \quad & (\mathcal{Q}_{V_{s,t}|\mathbf{Y},\mathbf{V}^{s-1}})_{t=1}^N = f_{\text{NN}}(\mathbf{y}, \mathbf{v}^{s-1}; \Theta) \end{aligned} \quad (46)$$

where  $\langle \cdot \rangle$  denotes Monte-Carlo averaging over  $N_{\text{blk}}$  transmit symbols and pairs  $(\mathbf{v}^{(w)}, \mathbf{y}^{(w)})_{w=1}^{N_{\text{blk}}}$ , and the APPs are a function of the NN  $f_{\text{NN}}(\mathbf{y}, \mathbf{v}^{s-1}; \Theta)$ . The solution to (46) is usually approximated by batch stochastic gradient descent (SGD).

#### D. Receiver Complexity

Table I compares the number of multiplications per symbol APP calculation for the FBA, bit-wise GS [9], and the NN. The FBA complexity is exponential in  $\tilde{K}$  (9). In contrast, the GS complexity is quadratic in  $\tilde{K}$  and linear in the number of bits per source symbol  $m$ , iterations  $N_{\text{iter}}$ , and parallel samplers  $N_{\text{par}}$ . Matrix-vector multiplications dominate the NN complexity, which depends on the number of NN layers and their sizes  $(\ell_i)_{i=1}^L$ . Note that we use real-valued NN inputs. For complex-valued inputs (36), composite real representations must be used, doubling the dimensions  $L_Y$  and  $L_{\text{IC}}$ . The FBA and GS also require complex multiplications when the modulation format and filters are complex-valued. We do not consider these cases in Table I.

## VI. NUMERICAL RESULTS

We study short-haul optical fiber links with a SLD, as described in Sec. II-B2. We compare the mismatched FBA, GS, and NN equalizers for bipolar and complex modulation alphabets; see [9], [23], [67], [85]. The program code is available at [86].

#### A. System Parameters

The system parameters are listed in Table II. The DAC performs sinc pulse shaping at the symbol rate 35 GBd. We consider  $L_{\text{fib}} = 0$  (back-to-back) and  $L_{\text{fib}} = 30$  km of SSMF without fiber attenuation. The  $L_{\text{fib}} = 0$  model is reasonable for several kilometers of fiber in the O-band where chromatic dispersion is low; see [87, Chap. 2.6.2]. The pulse shape and dispersion introduce long memory in the combined channel  $g(t)$ ; see Fig. 3. The SLD doubles the bandwidth of the signal  $X(t)$  to  $2B$ . The receive filter  $h(t)$  is a sinc pulse with

TABLE II  
SHORT-REACH FIBER-OPTIC SYSTEM [23, SEC. II A].

Parameters	
Fiber length	$L_{\text{fib}} \in \{0, 30 \text{ km}\}$
Attenuation factor	0 dB/km
Carrier wavelength	1550 nm (C band transmission)
Group velocity dispersion	$\beta_2 = -2.168 \cdot 10^{-23} \text{ s}^2/\text{km}$
Symbol rate	$B = 35 \text{ GBd}$
DAC and SSMF	$g(t) = B \cdot \text{sinc}(Bt) * g_{\text{SSMF}}(t)$
Frequency response of SSMF	$G_{\text{SSMF}}(f) = \exp(j\beta_2/2(2\pi f)^2 L_{\text{fib}})$
Receive photo-diode (SLD)	$\xi(x) =  x ^2$
Real-valued post-SLD AWGN	$N'(t)$ , PSD = $N_0/2$
Receive filter	$h(t) = 2B \text{sinc}(2Bt)$
Oversampling factors	$N_{\text{os}} = N_{\text{sim}} = 2$
Filtered and sampled noise	$N_k$ , AWGN with variance $\sigma^2 = N_0 B$

bandwidth  $2B$ , and oversampling  $Y(t)$  with  $N_{\text{os}} = 2$  provides sufficient statistics.

We approximate  $g(t)$  by a discrete filter  $g_k$  with  $K_g = 151 \cdot N_{\text{sim}} + 1$  taps, resulting in a memory of  $\tilde{K}_g = 151$  symbols. This choice has  $g_k$  containing 99.9% of the energy of  $g(t)$ . The receive filter  $h(t)$  does not influence the transmit signal component, and the discrete-time noise  $N_k$  is AWGN with variance  $\sigma^2$ . We thus have  $\tilde{K}_h = 0$  and the total system memory (9) is  $\tilde{K} = \tilde{K}_g$ . We simulate blocks with  $n \geq 20 \cdot 10^3$  symbols. The average transmit power is

$$P_{\text{tx}} = \frac{\mathbb{E}[\|X(t)\|^2]}{n \cdot T_s} \quad (47)$$

and the filtered noise variance is  $\sigma^2 = 1$  so  $\text{SNR} = P_{\text{tx}}$ . We use the  $M$ -ary modulations:

- unipolar  $M$ -PAM with  $\mathcal{A} = \{0, 1, \dots, 2^m - 1\}$ ;
- bipolar  $M$ -ASK with  $\mathcal{A} = \{\pm 1, \pm 3, \dots, \pm(2^m - 1)\}$ ;
- $M$ -SQAM [23] with  $\mathcal{A} = \{\pm a, \pm ja \mid a = 1, 2, \dots, M/4\}$

where SQAM refers to star-QAM. We use differential phase encoding before the DAC to help resolve phase ambiguities; see [9, Appendix]. The spectral efficiency in bit/s/Hz corresponds to the information rate in bpcu because the time-bandwidth product of the sinc pulse is 1.

#### B. NN Optimization

We optimize one NN per SIC stage and SNR. The NNs are initialized with optimized parameters from a lower SNR, if available<sup>2</sup>. We approximate (46) via batch SGD with moment extension, namely ADAM [88]. RNNs may experience numerical instabilities during SGD when the number  $N(S-s+1)$  of sequential inputs (41) is large [89]. During training, we limit the inputs to  $T_{\text{RNN}}$ , which results in  $N = T_{\text{RNN}}/(S-s+1)$  symbols per SIC stage. The number of inputs  $T_{\text{RNN}}$  and size  $L_Y$  indicate the maximum symbol memory that the RNN can capture and is approximately  $\tilde{N}_{\text{RNN}} \approx \lfloor L_Y/N_{\text{os}} \rfloor + (T_{\text{RNN}} - 1)$ .

We perform batch SGD with  $N_{\text{batch}}$  inputs and the strings  $(\mathbf{v}^{(w)}, \mathbf{y}^{(w)})_{w=1}^{N_{\text{batch}}}$  where  $N = T_{\text{RNN}}/(S-s+1)$ . We take  $N_{\text{iter}}$  gradient steps with step size<sup>3</sup>  $\beta_{\text{lr}}$ . To improve numerical stability at high SNR, the NN inputs (36) are normalized to unit

<sup>2</sup>The latest program version [86, v1.1] applies learning rate scheduling to train NNs faster and without initialization from a previous SNR.

<sup>3</sup>The decay rates for the gradient moment estimates are chosen as in [88].



TABLE III  
NN PARAMETERS.

Modulation		$L_Y, \ell_2, \ell_3, \ell_4, \ell_5$	$\bar{N}_{\text{RNN}}$	$L_{\text{IC}}$	$T_{\text{RNN}}$	$N_{\text{batch}}$	$N_{\text{blk}}$	$n$	$\beta_{\text{lr}}$	$N_{\text{iter}}$	$L_{\text{fib}}$ [km]
$M = 4$	—	32, 64	47	16	32	128	$1 \cdot 10^3$	$6 \cdot 10^4$	$1 \cdot 10^{-3}$	$1 \cdot 10^4$	0
$M = 8$	—	64, 128, 64	95	32	64	64	$3 \cdot 10^3$	$6 \cdot 10^4$	$5 \cdot 10^{-4}$	$6 \cdot 10^4$	0
$M = 16$	—	84, 128, 128	105	64	64	64	$3 \cdot 10^3$	$6 \cdot 10^4$	$2 \cdot 10^{-4}$	$6 \cdot 10^4$	0
$M = 32$	—	84, 128, 128	105	64	64	64	$3 \cdot 10^3$	$6 \cdot 10^4$	$1 \cdot 10^{-4}$	$6 \cdot 10^4$	0
$M = 64$	—	84, 128, 128, 128, 64	125	100	84	84	$3 \cdot 10^3$	$6 \cdot 10^4$	$5 \cdot 10^{-5}$	$7.5 \cdot 10^4$	0
$M = 128$	—	84, 128, 128, 128, 128	125	100	84	84	$3 \cdot 10^3$	$6 \cdot 10^4$	$5 \cdot 10^{-5}$	$7.5 \cdot 10^4$	0
$M = 4$	PAM/ASK	64, 128, 64	95	32	64	128	$1 \cdot 10^3$	$6 \cdot 10^4$	$5 \cdot 10^{-4}$	$2 \cdot 10^4$	30
$M = 4$	SQAM	64, 256, 128, 128	95	32	64	128	$1 \cdot 10^3$	$6 \cdot 10^4$	$5 \cdot 10^{-4}$	$2 \cdot 10^4$	30
$M = 8$	PAM/ASK	64, 128, 128	115	32	84	128	$1 \cdot 10^3$	$6 \cdot 10^4$	$3 \cdot 10^{-4}$	$5 \cdot 10^4$	30
$M = 8$	SQAM	64, 256, 128, 128	115	32	84	128	$1 \cdot 10^3$	$6 \cdot 10^4$	$3 \cdot 10^{-4}$	$5 \cdot 10^4$	30
$M = 16$	—	84, 200, 128, 128	161	64	120	64	$3 \cdot 10^3$	$8 \cdot 10^4$	$5 \cdot 10^{-5}$	$8 \cdot 10^4$	30
$M = 32$	—	100, 200, 200, 200, 168	169	64	120	64	$7 \cdot 10^3$	$8 \cdot 10^4$	$4 \cdot 10^{-5}$	$1 \cdot 10^5$	30
$M = 64$	—	100, 300, 300, 300, 240	169	100	120	64	$7 \cdot 10^3$	$8 \cdot 10^4$	$4 \cdot 10^{-5}$	$1 \cdot 10^5$	30

TABLE IV  
LIST OF NN SYMBOLS.

Description	Symbol	Occurrence
Number of layers	$L$	Fig. 7
Number of channel outputs	$L_Y$	(37)
Number of IC symbols	$L_{\text{IC}}$	(38)
Input size of first layer	$\ell_1 = L_Y + L_{\text{IC}}$	(36), Sec. V-B
Input size of layer $i$ , $1 \leq i \leq L$	$\ell_i$	Sec. V-B
Batch size for SGD	$N_{\text{batch}}$	Sec. VI-B
Step size for SGD	$\beta_{\text{lr}}$	Sec. VI-B
Number of SGD iterations	$N_{\text{iter}}$	Sec. VI-B
Number of sequential training inputs	$T_{\text{RNN}}$	Sec. VI-B
Time-varying period of NN	$\Gamma$	Sec. V-B
Approximate NN memory	$\bar{N}_{\text{RNN}}$	Sec. VI-B
Number of frames for validation	$N_{\text{blk}}$	Sec. VI-B
Number of symbols per frame	$n$	Sec. VI-B

variance. We use Monte-Carlo simulations to evaluate NN-SIC rates with  $N_{\text{blk}}$  frames, each having  $n$  symbols; see (45)-(46). The NN parameters are found empirically; see Table III. The symbols used for the NNs are summarized in Tab. IV. Table V and Fig. 8 show the algorithmic complexities for the examples of Sec. VI-C by listing the number of multiplications for the FBA, GS, and NNs for stage  $s = 1$ .

### C. SIC Rates

We plot the SIC rates in bits per channel use (bpcu) for the mismatched FBA [23], GS [9], and NN detectors. In general, the FBA must use a mismatched channel memory  $\bar{N} \ll \bar{K}$  because its complexity grows exponentially in  $\bar{K}$ ; see Tab. I. Similarly, we use a mismatched memory  $\bar{N} < \bar{K}$  for GS.

Consider 4-PAM/ASK/SQAM with FBA-SIC and NN-SIC. We compare rates with  $L_{\text{fib}} = 0$  and  $L_{\text{fib}} = 30$  km SSMF in Fig. 9 and Fig. 10, respectively. We compute the JDD upper bounds (UBs) of [83, Eq. (45)] by using the mismatched FBA with  $\bar{N} = 9$ , and where the auxiliary channel is optimized according to [23, Sec. III C]. The rates for bit-wise GS [9, Fig. 8] with  $\bar{N} = 9$ ,  $N_{\text{par}} = 20$ , and  $N_{\text{iter}} = 60$  are similar to the FBA-SIC rates. Observe from Table V and Fig. 8 that the algorithmic complexity remains large for the NN-based approach, which motivates looking for simplifications or alternative algorithms.

TABLE V  
NUMBER OF MULTIPLICATIONS PER APP ESTIMATE.

Parameters	FBA	GS	NN (real/complex)	
$M = 4$ $L_{\text{fib}} = 0$ km	Fig. 9	$1 \cdot 10^6$	$2 \cdot 10^5$	$5 \cdot 10^3$
$M = 8$	Fig. 16a	—	—	$3 \cdot 10^4$
$M = 16$	Fig. 16a	—	—	$6 \cdot 10^4$
$M = 32$	Fig. 12,14	—	$2 \cdot 10^7$	$6 \cdot 10^4$
$M = 64$	Fig. 16a	—	—	$1 \cdot 10^5$
$M = 128$	Fig. 16a	—	—	$1 \cdot 10^5$
$M = 4$ $L_{\text{fib}} = 30$ km	Fig. 10	$1 \cdot 10^6$	$2 \cdot 10^5$	$3 \cdot 10^4 / 1 \cdot 10^5$
$M = 8$	Fig. 11	$2 \cdot 10^7$	$2 \cdot 10^5$	$5 \cdot 10^4 / 1 \cdot 10^5$
$M = 16$	Fig. 16b	—	—	$1 \cdot 10^5$
$M = 32$	Fig. 13,15	—	$2 \cdot 10^7$	$2 \cdot 10^5$
$M = 64$	Fig. 16b	—	—	$5 \cdot 10^5$

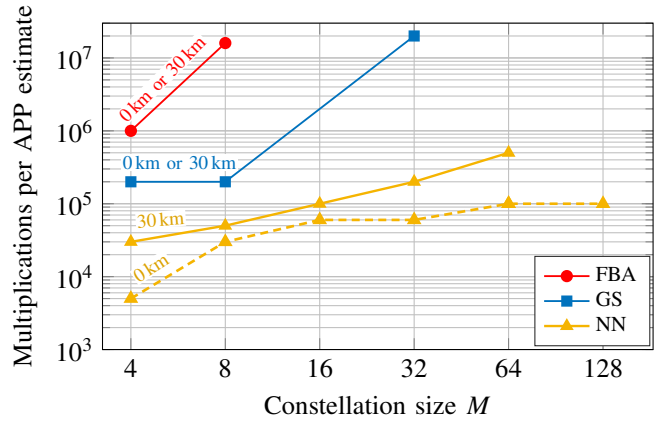


Fig. 8. Algorithmic complexity versus constellation size for SSMF lengths  $L_{\text{fib}} = 0$  km and  $L_{\text{fib}} = 30$  km.

Fig. 9 and Fig. 10 show that the rates increase with  $S$ . NN-SIC is at least as good as the mismatched FBA-SIC for all modulation formats. The NN shows large gains over the mismatched FBA for  $S > 2$  and medium to high SNRs because of the FBA channel mismatch, i.e., the FBA memory is much smaller than the NN memory; see the third column in Tab. III. For 4-PAM/ASK and  $L_{\text{fib}} = 0$ , the best NN curves reduce the gap to the UBs to 0.8 dB at around 80% of the maximum rate. The rates for 4-SQAM and  $L_{\text{fib}} = 0$  saturate early. This is likely due to phase symmetries in 4-SQAM; see [9, Appendix].

For  $L_{\text{fib}} = 30$  km, the gaps to the UB reduce to  $\approx 1$  dB for all modulations. For 4-SQAM, we had to use a larger NN than for 4-PAM/ASK; see Fig. 10. For  $L_{\text{fib}} = 0$  and  $L_{\text{fib}} = 30$  km, two and four SIC levels are needed to approach the JDD rate, respectively.

The NN outperforms GS and the mismatched FBA with much smaller complexity; see Table I and Fig. 8. For  $M = 4$  and  $L_{\text{fib}} = 0$ , the NN requires 40 times fewer multiplications than GS and 200 times fewer than the FBA. For real-valued modulation and  $L_{\text{fib}} = 30$  km, the NN is roughly ten times less complex than GS and 30 times less complex than the mismatched FBA. For 4-SQAM, the complexity of GS and the NN is similar. Fig. 11 shows similar results for 8-PAM/ASK/SQAM for  $L_{\text{fib}} = 30$  km, where we chose SIC with up to  $S = 6$  stages.

Fig. 12 and Fig. 13 compare the performance of NNs and bit-wise GS for 32-PAM/ASK/SQAM with  $L_{\text{fib}} = 0$  and  $S = 2$ , and  $L_{\text{fib}} = 30$  km and  $S = 6$ , respectively. The FBA is infeasible for large modulation alphabets. GS runs with  $N_{\text{par}} = 64$  samplers,  $\bar{N} = 21$ , and  $N_{\text{iter}} = 125$ . The first 25 iterations constitute the “burn-in” period and are discarded. The performance of the NN and GS match at low SNRs, except for 32-SQAM and  $L_{\text{fib}} = 30$  km where GS is slightly better. At high SNRs, GS stalls; see [25] and [9, Fig. 8]. The NN achieves the maximum rates for 32-PAM/ASK and saturates slightly earlier for 32-SQAM. The NN outperforms GS and is over 300 times less complex for  $L_{\text{fib}} = 0$  and roughly 100 times less complex for  $L_{\text{fib}} = 30$  km.

The results in Fig. 14-16 consider NN-SIC only because GS “stalls” and the FBA is infeasible. The rates for 32-PAM/ASK/SQAM,  $L_{\text{fib}} = 0$  and  $L_{\text{fib}} = 30$  km are shown in Fig. 14 and Fig. 15, respectively. We use SIC with up to six stages; the dashed black curves show the rates for stage six. For  $L_{\text{fib}} = 0$ , 32-ASK and 32-SQAM require two SIC stages to approach JDD performance, while 32-PAM performs well even with SDD. For  $L_{\text{fib}} = 30$  km, 32-PAM and 32-ASK require at least four stages, while 32-SQAM may need more than six SIC stages.

Fig. 16a compares NN-SIC rates for  $L_{\text{fib}} = 0$ ,  $S = 2$  and modulations up to  $M = 128$ . ASK/SQAM with NN-SIC achieves large energy gains over classic PAM. The gains increase with  $M$  and reach  $\approx 3$  dB for  $M = 128$ . Fig. 16b plots rates for  $L_{\text{fib}} = 30$  km,  $S = 6$  and modulations up to  $M = 64$ . The gains over PAM are  $\approx 2.1$  dB. The SQAM rates saturate because SQAM has phase symmetries; see [9, Appendix]. The NN complexity scales roughly linearly with the modulation alphabet size  $M$ .

#### D. Periodically Time-Varying RNNs

Fig. 17 and 18 compare the rates of the periodically time-varying RNNs to classic RNNs that use time-invariant recurrent cells  $(\vec{C}^i, \vec{C}^i)_{i=1}^{L-1}$  [80, Chap. 10]. The latter RNNs use the same configuration as their time-varying counterparts; see Tab. III. Thus, both structures have the same computational complexity. To illustrate the results, we consider 8-ASK and 8-SQAM for  $L_{\text{fib}} = 30$  km.

Fig. 17a compares the SIC rates for  $S = 1, 2, 6$ . For SDD ( $S = 1$ ) and  $S = 2$ , the proposed RNNs per SIC stage are the

same as classic RNNs [80, Chap. 10.3]. SIC with  $S = 2$  stages gains  $\approx 1.2$  dB over SDD for medium to high SNRs. Using  $S = 6$  stages almost doubles the energy gains to  $\approx 2.2$  dB and  $\approx 2.4$  dB at 2.6 bpcu and 2.8 bpcu, respectively. In contrast, operating classic RNNs with  $S = 6$  is suboptimal and the gains reduce to 1.6 dB and 1.4 dB over SDD at 2.6 bpcu and 2.8 bpcu respectively.

Fig. 17b compares the individual stage rates for  $S = 6$ . For  $s = 1$  and  $s = S$ , our RNNs are the same as classic RNNs because the time-varying period is  $\Gamma = 1$ ; cf. Sec. V. Therefore, the rates in these stages are equal. For time-varying RNNs, the rates  $I_{q,N,SIC}^s$  are non-decreasing in  $s$ . This is in contrast to classic RNNs, where for  $P_{\text{tx}} \geq 8$  dB the stage  $s = 2$  rate is smaller than the stage  $s = 1$  rate. In other words, classic RNNs are suboptimal because they cannot process cyclostationary inputs correctly and cannot account for the decoded a-priori information from previous SIC stages. The periodically time-varying RNNs are tailored to cyclostationary processing and thus achieve significant energy gains in stages  $s = 2, \dots, 5$  compared to classical RNNs.

Fig. 18 shows similar results for 8-SQAM, where periodically time-varying RNNs gain 1.1 dB over classic RNNs for  $S = 6$  and rates around 2.5 bpcu. More SIC stages may be required to approach JDD performance for higher modulation orders, channels with more memory, or stronger ISI. Periodically time-varying RNNs should be even more advantageous for such cases.

## VII. CONCLUSION

We designed time-varying RNN equalizers for SIC and showed that they outperform FBA-SIC and GS-SIC with substantially less complexity. We simulated NN-SIC rates up to 7 bpcu with 128-PAM/ASK/SQAM for short-reach fiber-optic links with a SLD. Moreover, bipolar ASK and complex modulations gain up to 3 dB over classic unipolar PAM.

For future work, we plan to verify the computed rates with realistic coded modulations as in [9]; we also plan to include probabilistic shaping. We further plan to investigate the robustness and generalization capabilities of NN-SIC with data from hardware experiments; see [51]. The NN-SIC receiver may be a candidate for optical short-range links with direct detection if high-speed optical modulators [90] are available. One may further explore NN-compression methods [91] to reduce the number of NN parameters; we expect that the NN sizes for the higher SIC stages can be reduced because much of the interference is known. Finally, one can mitigate phase symmetries by precoding; see [9, Appendix].

## ACKNOWLEDGMENT

The authors wish to thank M. Schädler, S. Calabrò, D. Lentner and the reviewers for helpful discussions.

## REFERENCES

- [1] D. Tse and P. Viswanath, *Fundamentals of Wireless Communication*. Cambridge University Press, 2005.
- [2] T. Eriksson, W. Cao, and C. Fager, “Nonlinear effects of wireless transceivers,” *Wiley 5G Ref: The Essential 5G Reference Online*, pp. 1–30, 2019.

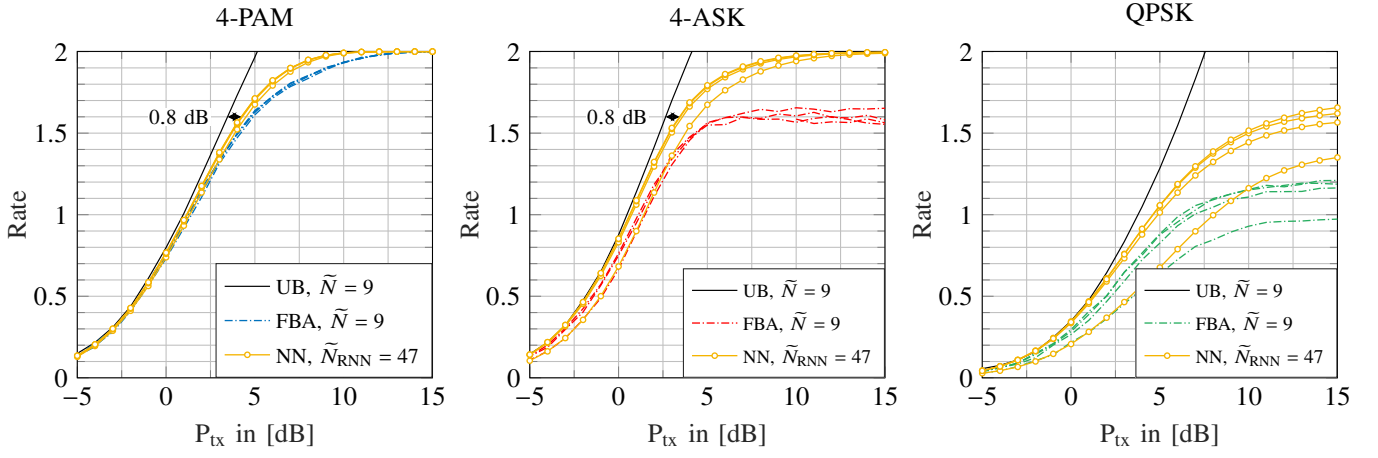


Fig. 9. SIC rates for  $L_{\text{fib}} = 0$  and  $S = 1, 2, 3, 4$  stages. Mismatched FBA and UB memory  $\tilde{N} = 9$ , RNN memory  $\tilde{N}_{\text{RNN}} = 47$ . The lower curves of a particular style show the SDD ( $S = 1$ ) rates, while the upper curves show the  $S = 4$  rates.

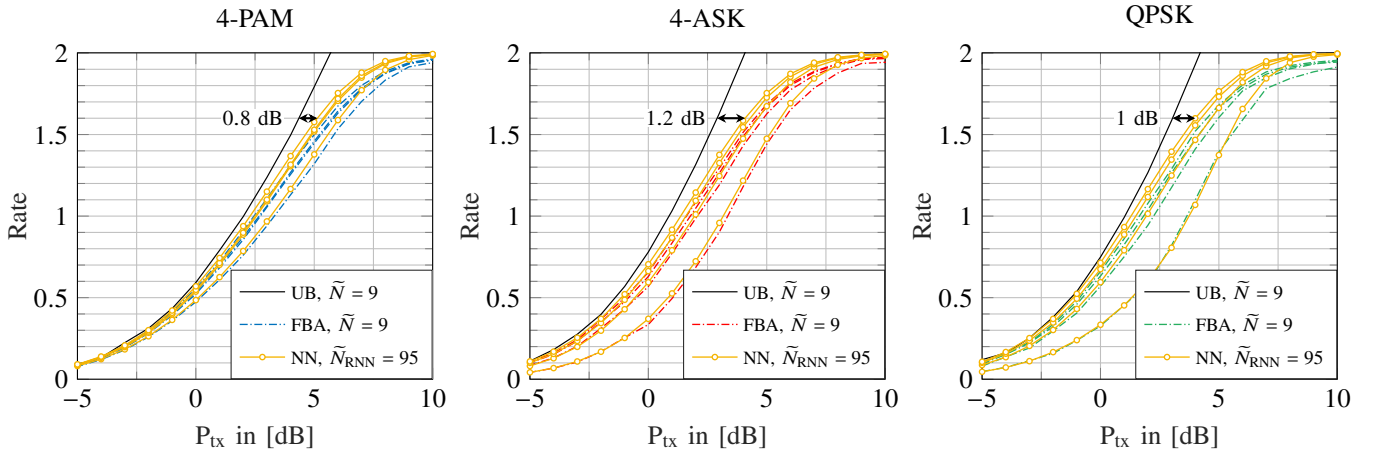


Fig. 10. SIC rates for  $L_{\text{fib}} = 30$  km and  $S = 1, 2, 3, 4$  stages. Mismatched FBA and UB memory  $\tilde{N} = 9$ , RNN memory  $\tilde{N}_{\text{RNN}} = 95$ . The lower curves of a particular style show the SDD ( $S = 1$ ) rates, while the upper curves show the  $S = 4$  rates.

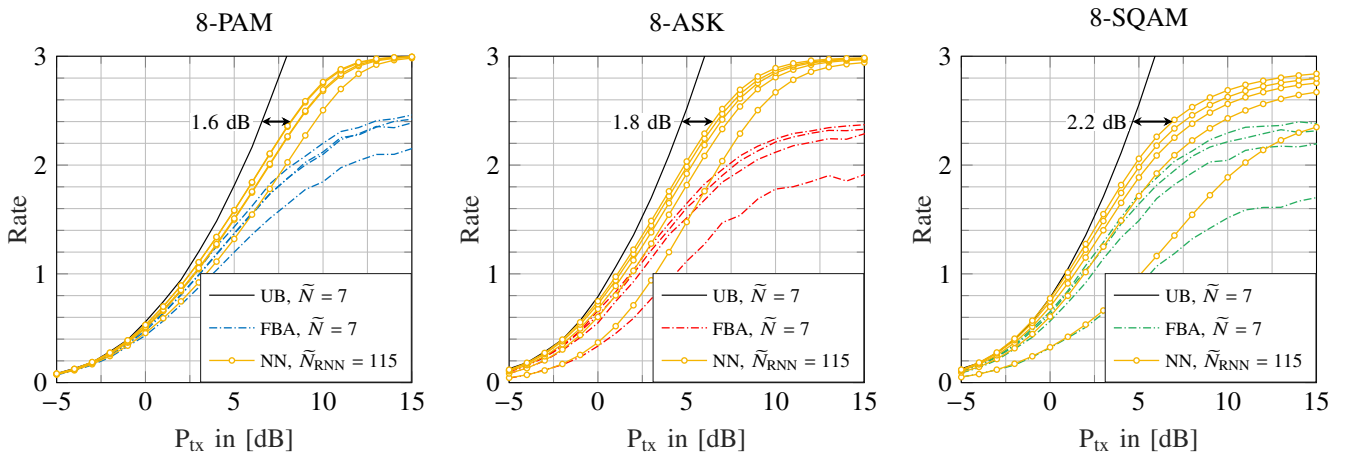


Fig. 11. SIC rates for  $L_{\text{fib}} = 30$  km,  $S = 1, 2, 3, 4$  stages and an additional plot with  $S = 6$  stages for the NN. Mismatched FBA and UB memory  $\tilde{N} = 7$ , RNN memory  $\tilde{N}_{\text{RNN}} = 115$ . The lower curves of a particular style show the SDD ( $S = 1$ ) rates, while the upper curves show the largest  $S$  rates.

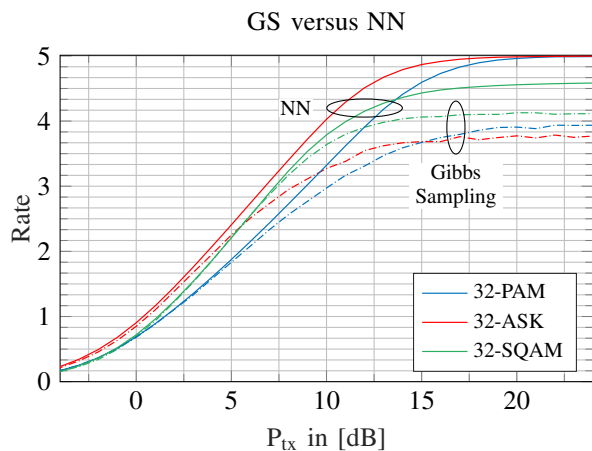


Fig. 12. SIC rates for  $L_{\text{fib}} = 0$  and  $S = 2$ . RNN:  $\tilde{N}_{\text{RNN}} = 105$ . Bit-wise GS [9]:  $\tilde{N} = 21$ ,  $N_{\text{iter}} = 125$  and  $N_{\text{par}} = 64$ .

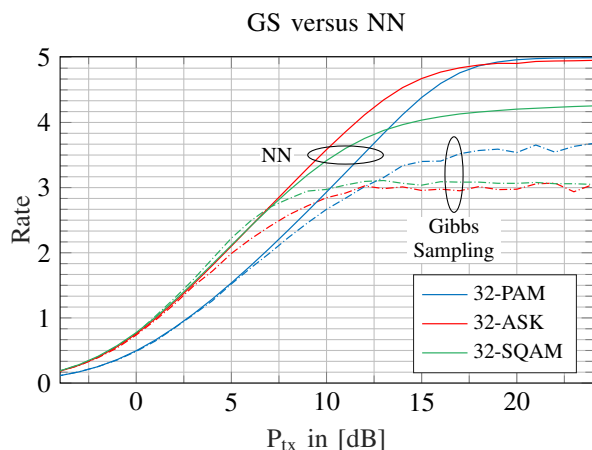


Fig. 13. SIC rates for  $L_{\text{fib}} = 30$  km and  $S = 6$ . RNN:  $\tilde{N}_{\text{RNN}} = 169$ . Bit-wise GS [9]:  $\tilde{N} = 21$ ,  $N_{\text{iter}} = 125$  and  $N_{\text{par}} = 64$ .

[3] C. Mollén, *On massive MIMO Base Stations with Low-end Hardware*. Linköping University Electronic Press, 2016, vol. 1756.

[4] M. Chagnon, "Optical communications for short reach," *J. Lightw. Technol.*, vol. 37, no. 8, pp. 1779–1797, April 2019.

[5] S. Merchan, A. Armada, and J. Garcia, "OFDM performance in amplifier nonlinearity," *IEEE Trans. Broad.*, vol. 44, no. 1, pp. 106–114, 1998.

[6] R. Müller and W. Gerstacker, "On the capacity loss due to separation of detection and decoding," *IEEE Trans. Inf. Theory*, vol. 50, no. 8, pp. 1769–1778, 2004.

[7] A. Sheikh, A. Graell i Amat, and G. Liva, "Achievable information rates for coded modulation with hard decision decoding for coherent fiber-optic systems," *J. Lightw. Technol.*, vol. 35, no. 23, pp. 5069–5078, 2017.

[8] G. Liga, A. Alvarado, E. Agrell, and P. Bayvel, "Information rates of next-generation long-haul optical fiber systems using coded modulation," *J. Lightw. Technol.*, vol. 35, no. 1, pp. 113–123, 2017.

[9] T. Prinz, D. Plabst, T. Wiegart, S. Calabrò, N. Hanik, and G. Kramer, "Successive interference cancellation for bandlimited channels with direct detection," *IEEE Trans. Commun.*, vol. 72, no. 3, pp. 1330–1340, 2024.

[10] C. Douillard, M. Jézéquel, C. Berrou, D. Electronique, A. Picart, P. Didier, and A. Glavieux, "Iterative correction of intersymbol interference: turbo-equalization," *Eur. Trans. Telecommun.*, vol. 6, no. 5, pp. 507–511, 1995.

[11] P. D. Alexander, A. J. Grant, and M. C. Reed, "Iterative detection in code-division multiple-access with error control coding," *Eur. Trans. Telecommun.*, vol. 9, no. 5, pp. 419–425, 1998.

[12] X. Wang and H. V. Poor, "Iterative (turbo) soft interference cancellation and decoding for coded CDMA," *IEEE Trans. Commun.*, vol. 47, no. 7, pp. 1046–1061, 1999.

[13] U. Wachsmann, R. F. Fischer, and J. B. Huber, "Multilevel codes: Theoretical concepts and practical design rules," *IEEE Trans. Inf. Theory*, vol. 45, no. 5, pp. 1361–1391, 1999.

[14] H. Pfister, J. Soriaga, and P. Siegel, "On the achievable information rates of finite state ISI channels," in *IEEE Global Telecommun. Conf.*, vol. 5, 2001, pp. 2992–2996 vol.5.

[15] J. B. Soriaga, H. D. Pfister, and P. H. Siegel, "Determining and approaching achievable rates of binary intersymbol interference channels using multistage decoding," *IEEE Trans. Inf. Theory*, vol. 53, no. 4, pp. 1416–1429, 2007.

[16] S. ten Brink, G. Kramer, and A. Ashikhmin, "Design of low-density parity-check codes for modulation and detection," *IEEE Trans. Commun.*, vol. 52, no. 4, pp. 670–678, 2004.

[17] L. Bahl, J. Cocke, F. Jelinek, and J. Raviv, "Optimal decoding of linear codes for minimizing symbol error rate," *IEEE Trans. Inf. Theory*, vol. 20, no. 2, pp. 284–287, 1974.

[18] J. Hagenauer and P. Hoehner, "A Viterbi algorithm with soft-decision outputs and its applications," in *IEEE Global Telecommun. Conf.*, 1989, pp. 1680–1686 vol.3.

[19] F. Kschischang, B. Frey, and H.-A. Loeliger, "Factor graphs and the sum-product algorithm," *IEEE Trans. Inf. Theory*, vol. 47, no. 2, pp. 498–519, 2001.

[20] D. J. C. MacKay, *Information Theory, Inference and Learning Algorithms*. Cambridge University Press, 2003.

[21] J. Cioffi, G. Dudevoir, M. Vedat Eyuboglu, and G. Forney, "MMSE decision-feedback equalizers and coding. I. Equalization results," *IEEE Trans. Commun.*, vol. 43, no. 10, pp. 2582–2594, 1995.

[22] T. Koh and E. Powers, "Second-order Volterra filtering and its application to nonlinear system identification," *IEEE Trans. Acoustics, Speech, and Signal Proc.*, vol. 33, no. 6, pp. 1445–1455, 1985.

[23] D. Plabst, T. Prinz, T. Wiegart, T. Rahman, N. Stojanović, S. Calabrò, N. Hanik, and G. Kramer, "Achievable rates for short-reach fiber-optic channels with direct detection," *J. Lightw. Technol.*, vol. 40, no. 12, pp. 3602–3613, 2022.

[24] F. Rusek and A. Prlja, "Optimal channel shortening for MIMO and ISI channels," *IEEE Trans. Wireless Commun.*, vol. 11, no. 2, pp. 810–818, 2012.

[25] M. Senst and G. Ascheid, "A Rao-Blackwellized Markov chain Monte Carlo algorithm for efficient MIMO detection," in *IEEE Int. Conf. Commun. (ICC)*. IEEE, 2011, pp. 1–6.

[26] C. Yin, W. Feng, J. Li, X. Bao, and G. Li, "Soft-input soft-output block decision feedback equalization for ISI channels," *IEEE Trans. Commun.*, vol. 69, no. 9, pp. 6213–6224, 2021.

[27] S. Liu and Z. Tian, "Near-optimum soft decision equalization for frequency selective MIMO channels," *IEEE Trans. Signal Proc.*, vol. 52, no. 3, pp. 721–733, 2004.

[28] X.-A. Wang and S. Wicker, "An artificial neural net Viterbi decoder," *IEEE Trans. Commun.*, vol. 44, no. 2, pp. 165–171, 1996.

[29] N. Shlezinger, N. Farsad, Y. C. Eldar, and A. J. Goldsmith, "Viterbinet: A deep learning based Viterbi algorithm for symbol detection," *IEEE Trans. Wireless Commun.*, vol. 19, no. 5, pp. 3319–3331, 2020.

[30] H. Kim, S. Oh, and P. Viswanath, "Physical layer communication via deep learning," *IEEE J. Sel. Areas Inf. Theory*, vol. 1, no. 1, pp. 5–18, 2020.

[31] Y. Jiang, H. Kim, H. Asnani, S. Kannan, S. Oh, and P. Viswanath, "Learn codes: Inventing low-latency codes via recurrent neural networks," in *IEEE Int. Conf. Commun. (ICC)*, 2019, pp. 1–7.

[32] S. Haykin, "Adaptive digital communication receivers," *IEEE Communications Magazine*, vol. 38, no. 12, pp. 106–114, 2000.

[33] T. Gruber, S. Cammerer, J. Hoydis, and S. t. Brink, "On deep learning-based channel decoding," in *Annu. Conf. Inf. Sci. Sys. (CISS)*, 2017, pp. 1–6.

[34] E. Nachmani, Y. Be'ery, and D. Burshtein, "Learning to decode linear codes using deep learning," in *Annu. Allerton Conf. Commun., Control, and Computing*, 2016, pp. 341–346.

[35] J. Bruck and M. Blaum, "Neural networks, error-correcting codes, and polynomials over the binary n-cube," *IEEE Trans. Inf. Theory*, vol. 35, no. 5, pp. 976–987, 1989.

[36] Y. Jiang, S. Kannan, H. Kim, S. Oh, H. Asnani, and P. Viswanath, "Deepturbo: Deep turbo decoder," in *IEEE Int. Workshop Signal Proc. Advances in Wireless Commun. (SPAWC)*, 2019, pp. 1–5.

[37] Y. Jiang, H. Kim, H. Asnani, S. Kannan, S. Oh, and P. Viswanath, "Turbo autoencoder: Deep learning based channel codes for point-to-point communication channels," in *Advances in Neural Inform. Proc.*

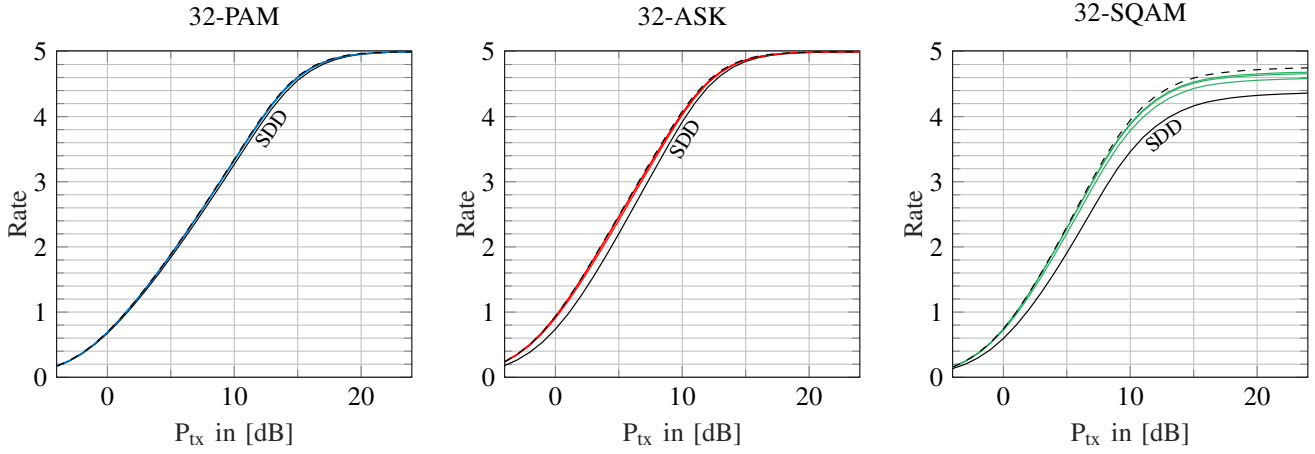


Fig. 14. SIC rates with  $S = 1, 2, 3, 4, 6$ ,  $L_{\text{fib}} = 0$  and  $\tilde{N}_{\text{RNN}} = 105$ . The lower curves show the SDD ( $S = 1$ ) rates, while the upper curves show the  $S = 6$  rates.

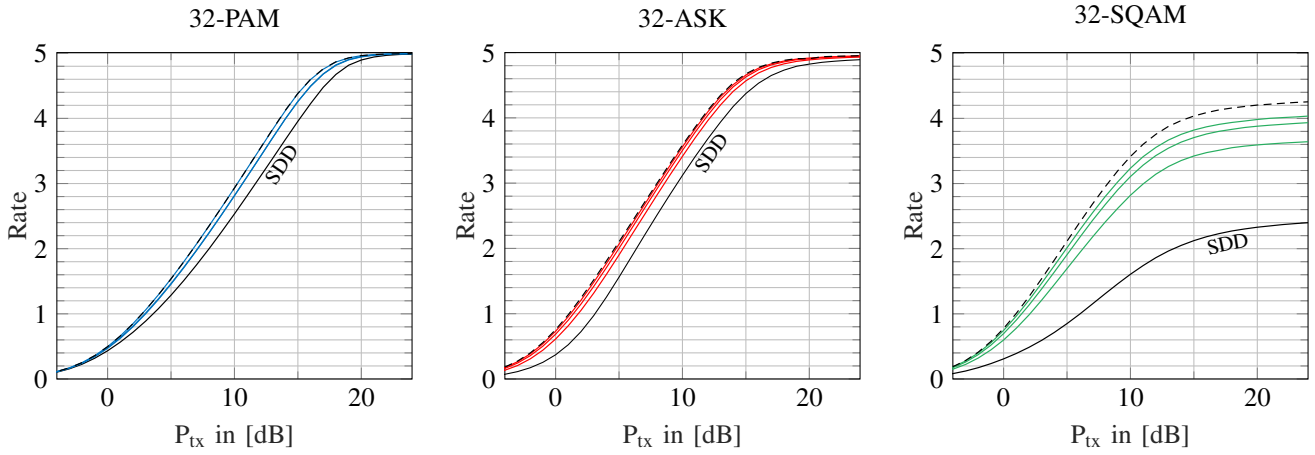


Fig. 15. SIC rates with  $S = 1, 2, 3, 4, 6$ ,  $L_{\text{fib}} = 30$  km and  $\tilde{N}_{\text{RNN}} = 169$ . The lower curves show the SDD ( $S = 1$ ) rates, while the upper curves show the  $S = 6$  rates.

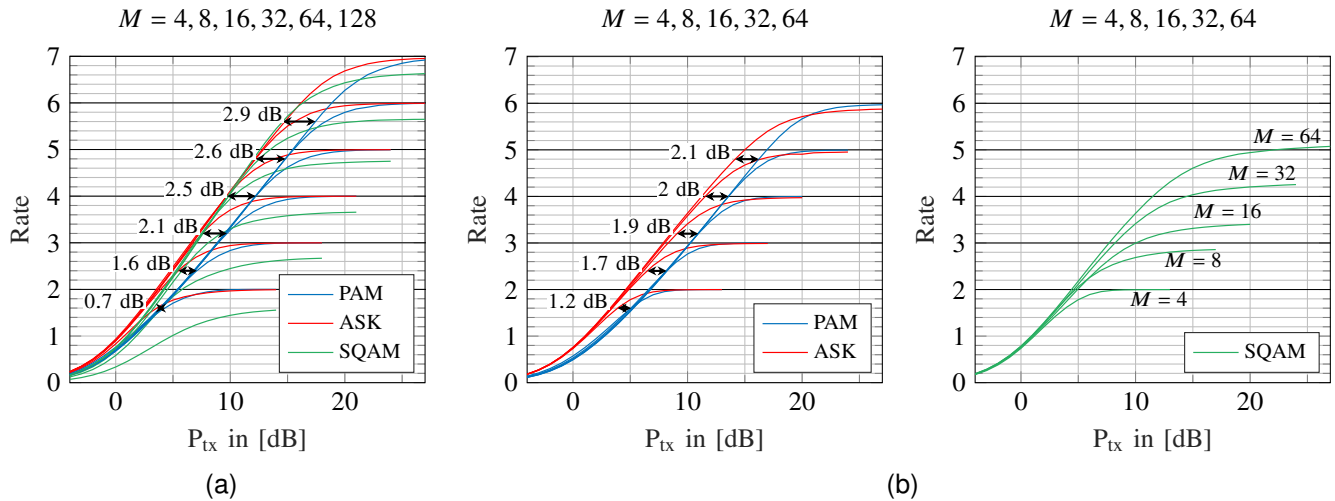


Fig. 16. SIC rates for (a)  $L_{\text{fib}} = 0$  and  $S = 2$  and (b)  $L_{\text{fib}} = 30$  km and  $S = 6$ .

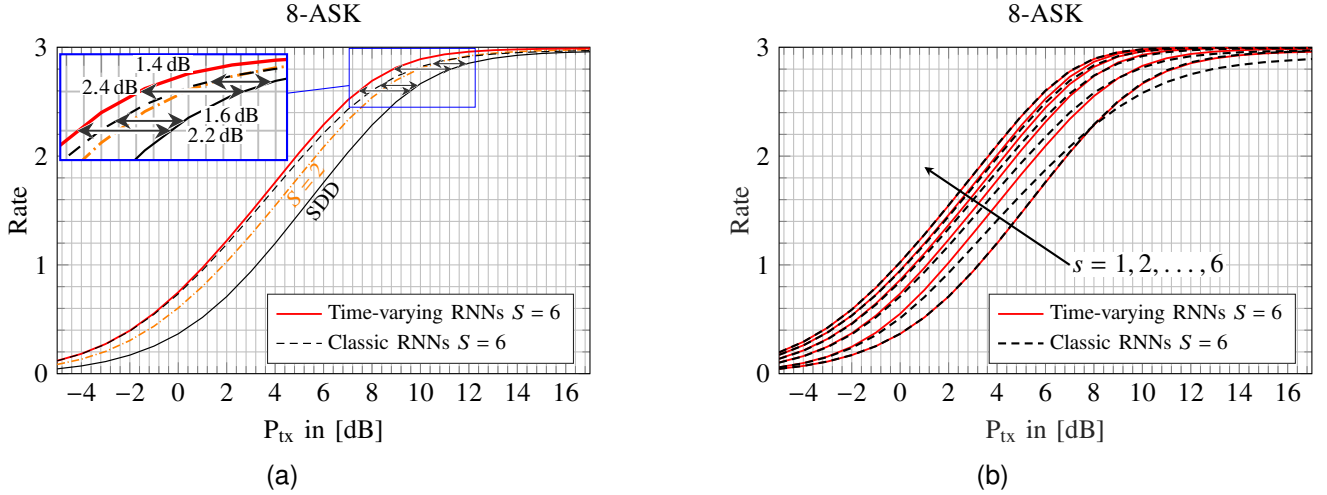


Fig. 17. Time-varying RNNs vs. classic RNNs for 8-ASK and  $L_{\text{fib}} = 30\text{km}$ : (a) SIC rates for  $S = 1, 2, 6$ ; (b) individual stage rates  $I_{q,N,\text{SIC}}^S$  for  $S = 6$ .

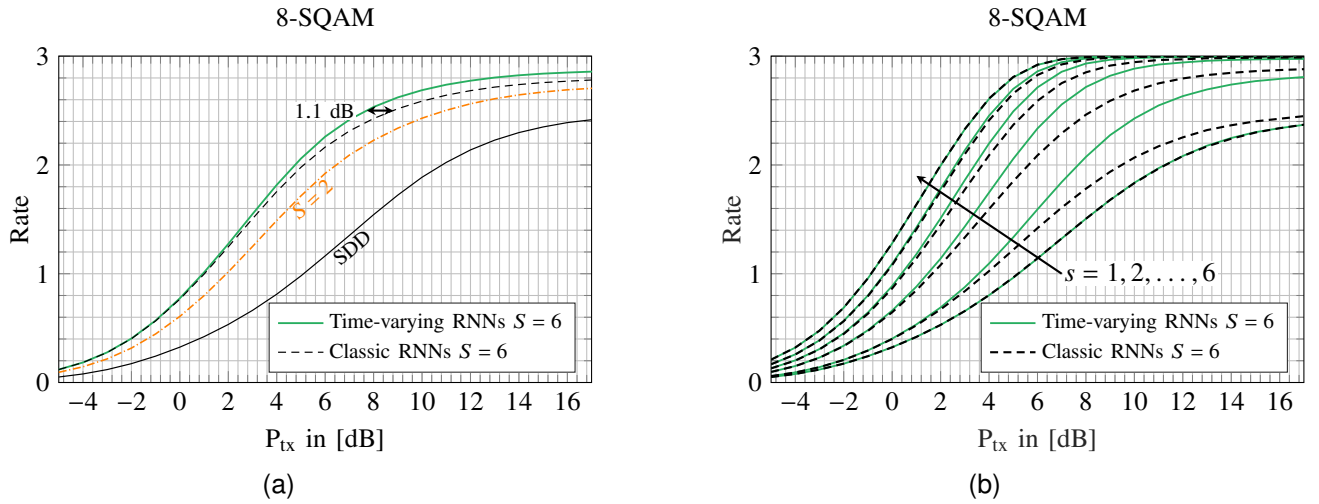


Fig. 18. Time-varying RNNs vs. classic RNNs for 8-SQAM and  $L_{\text{fib}} = 30\text{km}$ : (a) SIC rates for  $S = 1, 2, 6$ ; (b) individual stage rates  $I_{q,N,\text{SIC}}^S$  for  $S = 6$ .

- Systems, H. Wallach, H. Larochele, A. Beygelzimer, F. d'Alché-Buc, E. Fox, and R. Garnett, Eds., vol. 32. Curran Associates, Inc., 2019.
- [38] J. Clausius, S. Dörner, S. Cammerer, and S. t. Brink, "Serial vs. parallel turbo-autoencoders and accelerated training for learned channel codes," in *Int. Symp. Topics in Coding (ISTC)*, 2021, pp. 1–5.
- [39] H. Ye and G. Y. Li, "Initial results on deep learning for joint channel equalization and decoding," in *IEEE Vehic. Technol. Conf. (VTC-Fall)*, 2017, pp. 1–5.
- [40] Y. Zhang, H. Wu, and M. Coates, "On the design of channel coding autoencoders with arbitrary rates for ISI channels," *IEEE Wireless Commun. Lett.*, vol. 11, no. 2, pp. 426–430, 2022.
- [41] C. Han, H. Zhao, Z. Chen, and F. Wang, "Sparse neural network for detection and decoding of non-binary polar-coded SCMA," *IEEE Trans. Wireless Commun.*, pp. 1–1, 2022.
- [42] S. Dörner, S. Rottacker, M. Gauger, and S. t. Brink, "Bit-wise autoencoder for multiple antenna systems," in *Int. Symp. Wireless Commun. Systems (ISWCS)*, 2021, pp. 1–5.
- [43] W. Xu, Z. Zhong, Y. Be'ery, X. You, and C. Zhang, "Joint neural network equalizer and decoder," in *Int. Symp. Wireless Commun. Systems (ISWCS)*, 2018, pp. 1–5.
- [44] Y. Liao, N. Farsad, N. Shlezinger, Y. C. Eldar, and A. J. Goldsmith, "Deep neural network symbol detection for millimeter wave communications," in *2019 IEEE Global Commun. Conf. (GLOBECOM)*, 2019, pp. 1–6.
- [45] M. Honkala, D. Korpi, and J. M. J. Huttunen, "Deeprx: Fully convolutional deep learning receiver," *IEEE Trans. Wireless Commun.*, vol. 20, no. 6, pp. 3925–3940, 2021.
- [46] M. B. Fischer, S. Dörner, F. Krieg, S. Cammerer, and S. t. Brink, "Adaptive NN-based OFDM receivers: Computational complexity vs. achievable performance," in *Asilomar Conf. Sign., Syst., and Comp.*, 2022, pp. 194–199.
- [47] N. Samuel, T. Diskin, and A. Wiesel, "Learning to detect," *IEEE Trans. Signal Proc.*, vol. 67, no. 10, pp. 2554–2564, 2019.
- [48] T. Uhlemann, S. Cammerer, A. Span, S. Doerner, and S. ten Brink, "Deep-learning autoencoder for coherent and nonlinear optical communication," in *Photonic Networks; 21th ITG-Symp.*, 2020, pp. 1–8.
- [49] C. Häger, H. D. Pfister, R. M. Büttler, G. Liga, and A. Alvarado, "Model-based machine learning for joint digital backpropagation and PMD compensation," in *2020 Optical Fiber Communications Conference and Exhibition (OFC)*, 2020, pp. 1–3.
- [50] R. M. Büttler, C. Häger, H. D. Pfister, G. Liga, and A. Alvarado, "Model-based machine learning for joint digital backpropagation and PMD compensation," *Journal of Lightwave Technology*, vol. 39, no. 4, pp. 949–959, 2021.
- [51] B. Karanov, M. Chagnon, F. Thouin, T. A. Eriksson, H. Bülow, D. Lavery, P. Bayvel, and L. Schmalen, "End-to-end deep learning of optical fiber communications," *J. Lightw. Technol.*, vol. 36, no. 20, pp. 4843–4855, 2018.
- [52] B. Karanov, D. Lavery, P. Bayvel, and L. Schmalen, "End-to-end optimized transmission over dispersive intensity-modulated channels using bidirectional recurrent neural networks," *Opt. Express*, vol. 27, no. 14, pp. 19 650–19 663, Jul 2019.
- [53] N. Shlezinger, R. Fu, and Y. C. Eldar, "Deep soft interference cancel-

- lation for MIMO detection,” in *IEEE Int. Conf. Acoustics, Speech and Signal Proc. (ICASSP)*, 2020, pp. 8881–8885.
- [54] W.-J. Choi, K.-W. Cheong, and J. Cioffi, “Iterative soft interference cancellation for multiple antenna systems,” in *IEEE Wireless Commun. Netw. Conf.*, vol. 1, 2000, pp. 304–309 vol.1.
- [55] S. Baumgartner, O. Lang, and M. Huemer, “A soft interference cancellation inspired neural network for SC-FDE,” in *IEEE Int. Workshop Signal Proc. Advances in Wireless Commun. (SPAWC)*, 2022, pp. 1–5.
- [56] W.-C. Tsai, C.-F. Teng, H.-M. Ou, and A.-Y. A. Wu, “Neural network-aided BCJR algorithm for joint symbol detection and channel decoding,” in *2020 IEEE Workshop Signal Proc. Systems*, 2020, pp. 1–6.
- [57] C. Xu, T. Van Luong, L. Xiang, S. Sugiura, R. G. Maunder, L.-L. Yang, and L. Hanzo, “Turbo detection aided autoencoder for multicarrier wireless systems: Integrating deep learning into channel coded systems,” *IEEE Trans. Cognitive Commun. Netw.*, vol. 8, no. 2, pp. 600–614, 2022.
- [58] S. Dörner, J. Clausius, S. Cammerer, and S. t. Brink, “Learning joint detection, equalization and decoding for short-packet communications,” *IEEE Trans. Commun.*, vol. 71, no. 2, pp. 837–850, 2023.
- [59] M.-H. Yang, J.-L. Chen, and P.-Y. Cheng, “Successive interference cancellation receiver with neural network compensation in the CDMA systems,” in *Asilomar Conf. Sign., Syst., and Comp.*, vol. 2, 2000, pp. 1417–1420 vol.2.
- [60] C. Lin, Q. Chang, and X. Li, “A deep learning approach for MIMO-NOMA downlink signal detection,” *Sensors*, vol. 19, no. 11, p. 2526, 2019.
- [61] J.-M. Kang, I.-M. Kim, and C.-J. Chun, “Deep learning-based MIMO-NOMA with imperfect SIC decoding,” *IEEE Systems J.*, vol. 14, no. 3, pp. 3414–3417, 2020.
- [62] M. A. Aref and S. K. Jayaweera, “Deep learning-aided successive interference cancellation for MIMO-NOMA,” in *IEEE Global Commun. Conf.*, 2020, pp. 1–5.
- [63] J. Kim, J. Kim, and M.-S. Lee, “Enhanced deep soft interference cancellation for multiuser symbol detection,” *ETRI Journal*, 2023.
- [64] T. Van Luong, N. Shlezinger, C. Xu, T. M. Hoang, Y. C. Eldar, and L. Hanzo, “Deep learning based successive interference cancellation for the non-orthogonal downlink,” *IEEE Trans. Vehic. Technol.*, vol. 71, no. 11, pp. 11 876–11 888, 2022.
- [65] X. Yang, S. Houcke, C. Laot, and H. Wang, “Soft decision feedback equalizer for channels with low SNR in underwater acoustic communications,” in *2MTS/IEEE OCEANS - Bergen*, 2013, pp. 1–5.
- [66] D. Plabst, T. Prinz, F. Diedolo, T. Wiegart, G. Böcherer, N. Hanik, and G. Kramer, “Neural network equalizers and successive interference cancellation for bandlimited channels with a nonlinearity,” in *IEEE Int. Symp. Inf. Theory*, to appear.
- [67] A. Tasbihi and F. R. Kschischang, “Direct detection under Tukey signalling,” *J. Lightw. Technol.*, vol. 39, no. 21, pp. 6845–6857, 2021.
- [68] T. M. Cover and J. A. Thomas, *Elements of Information Theory*, 2nd ed. John Wiley & Sons, Inc., Hoboken, NJ, USA, 2006.
- [69] H. Friis, “Noise figures of radio receivers,” *Proc. IRE*, vol. 32, no. 7, pp. 419–422, 1944.
- [70] C. Rapp, “Effects of HPA-nonlinearity on a 4-DPSK/OFDM-signal for a digital sound broadcasting signal,” *ESA Special Publication*, vol. 332, pp. 179–184, 1991.
- [71] A. Saleh, “Frequency-independent and frequency-dependent nonlinear models of TWT amplifiers,” *IEEE Trans. Commun.*, vol. 29, no. 11, pp. 1715–1720, 1981.
- [72] A. Ghorbani and M. Sheikhan, “The effect of solid state power amplifiers (SSPAs) nonlinearities on MPSK and M-QAM signal transmission,” in *Int. Conf. Digital Proc. Signals in Commun.*, 1991, pp. 193–197.
- [73] D. Plabst, F. J. García-Gómez, T. Wiegart, and N. Hanik, “Wiener filter for short-reach fiber-optic links,” *IEEE Commun. Lett.*, vol. 24, no. 11, pp. 2546–2550, 2020.
- [74] G. T. Zhou and R. Raich, “Spectral Analysis of Polynomial Nonlinearity with Applications to RF Power Amplifiers,” *EURASIP J. Applied Signal Proc.*, vol. 2004, p. 256395, Dec. 2004.
- [75] G. Wise, A. Traganitis, and J. Thomas, “The effect of a memoryless nonlinearity on the spectrum of a random process,” *IEEE Trans. Inf. Theory*, vol. 23, no. 1, pp. 84–89, 1977.
- [76] H. Ochiai, “An analysis of band-limited communication systems from amplifier efficiency and distortion perspective,” *IEEE Trans. Commun.*, vol. 61, no. 4, pp. 1460–1472, 2013.
- [77] J. Huber, “Trelliscodierte digitale Übertragungsverfahren,” in *Trellis-codierung*. Springer, 1992, pp. 141–260.
- [78] F. Schuh, A. Schenk, and J. B. Huber, “Reduced complexity super-trellis decoding for convolutionally encoded transmission over ISI-channels,” in *Int. Conf. Comp., Netw., and Commun. (ICNC)*, 2013, pp. 484–489.
- [79] T. R. Giallorenzi and S. G. Wilson, “Multiuser ML sequence estimator for convolutionally coded asynchronous DS-CDMA systems,” *IEEE Trans. Commun.*, vol. 44, no. 8, pp. 997–1008, 1996.
- [80] I. Goodfellow, Y. Bengio, and A. Courville, *Deep learning*. MIT press, 2016.
- [81] K. Fukushima, “Visual feature extraction by a multilayered network of analog threshold elements,” *IEEE Trans. Systems Sci. and Cybernetics*, vol. 5, no. 4, pp. 322–333, 1969.
- [82] C. M. Bishop and N. M. Nasrabadi, *Pattern Recognition and Machine Learning*. Springer, 2006, vol. 4, no. 4.
- [83] D. M. Arnold, H.-A. Loeliger, P. O. Vontobel, A. Kavčić, and W. Zeng, “Simulation-based computation of information rates for channels with memory,” *IEEE Trans. Inf. Theory*, vol. 52, no. 8, pp. 3498–3508, 2006.
- [84] G. Böcherer, “Lecture Notes on Machine Learning for Communications,” <http://www.georg-boecherer.de/mlcomm.pdf>, Nov. 2021, [Online; accessed 20-April-2023].
- [85] A. Mecozi and M. Shttaif, “Information capacity of direct detection optical transmission systems,” *J. Lightw. Technol.*, vol. 36, no. 3, pp. 689–694, 2018.
- [86] D. Plabst. (2024) NN-MI: Neural Network Achievable Information Rate Computation for Channels with Memory. [Online]. Available: <https://github.com/DPlabst/NN-MI>
- [87] T. Schneider, *Nonlinear Optics in Telecommunications*, 1st ed. Springer-Verlag Berlin Heidelberg GmbH, 2004.
- [88] D. P. Kingma and J. Ba, “Adam: A method for stochastic optimization,” *arXiv preprint arXiv:1412.6980*, 2017.
- [89] R. Pascanu, T. Mikolov, and Y. Bengio, “On the difficulty of training recurrent neural networks,” 2013.
- [90] D. Moor, J. Leuthold, Y. Fedoryshyn, M. Möller, and U. Koch, “Plasmonic transceivers for the terahertz age,” *IEEE Sel. Top. Quan. Elec.*, vol. 30, no. 4: Adv. Mod. and Int. beyond Si and InP-based Plt., pp. 1–11, 2024.
- [91] J. O. Neill, “An overview of neural network compression,” *arXiv preprint arXiv:2006.03669*, 2020.